bioRxiv preprint doi: https://doi.org/10.1101/2021.08.11.455980; this version posted August 11, 2021. The copyright holder for this preprint (which was not certified by peer review) is the author/funder, who has granted bioRxiv a license to display the preprint in perpetuity. It is made available under aCC-BY-NC-ND 4.0 International license.

Nuclear SUN1 stabilizes endothelial cell junctions to regulate blood vessel formation

Danielle B Buglak[a], Ariel L Gold[b], Allison P Marvin[b], Shea N Ricketts[c], Morgan Oatley[b], Natalie T Tanke[a], Bryan N Johnson[b], and Victoria L Bautch[a,b,d,#]

[a]Curriculum in Cell Biology and Physiology, The University of North Carolina at Chapel Hill, Chapel Hill, North Carolina 27599, USA.
[b]Department of Biology, The University of North Carolina at Chapel Hill, Chapel Hill, North Carolina 27599, USA.
[c]Department of Pathology, The University of North Carolina at Chapel Hill, Chapel Hill, North Carolina 27599, USA.
[d]McAllister Heart Institute, The University of North Carolina at Chapel Hill, Chapel Hill, North Carolina 27599, USA

[#]Corresponding author: Victoria L Bautch, PhD
Professor of Biology
Department of Biology, CB#3280
University of North Carolina at Chapel Hill
Chapel Hill, NC 27599 USA
E-mail: bautch@med.unc.edu

Running head: Sun1 Regulates Endothelial Junctions and Angiogenesis

Abstract: 158 words
Text: 32,870 characters
Figures: 6 main, 5 supplemental
References: 71

bioRxiv preprint doi: https://doi.org/10.1101/2021.08.11.455980; this version posted August 11, 2021. The copyright holder for this preprint (which was not certified by peer review) is the author/funder, who has granted bioRxiv a license to display the preprint in perpetuity. It is made available under aCC-BY-NC-ND 4.0 International license.

SUMMARY

The nuclear membrane protein SUN1 promotes blood vessel formation and barrier function by stabilizing endothelial cell-cell junctions. Communication between SUN1 and endothelial cell junctions relies upon microtubules, revealing long-range cellular communication that is important for vascular development and function.

ABSTRACT

Endothelial cells line all blood vessels and coordinate blood vessel formation and the blood-tissue barrier via endothelial cell-cell junctions. The nucleus also regulates endothelial cell behaviors, but the mechanisms are poorly understood. Here we show that nuclear-localized SUN1, a LINC complex component that connects the nucleus to the cytoskeleton, regulates endothelial cell-cell junction communication and blood vessel formation. Loss of murine endothelial *Sun1* impaired blood vessel formation and destabilized junctions. At the cellular level, SUN1 stabilized endothelial cell-cell junctions and promoted barrier function. Abnormal SUN1-depleted junctions resembled those seen with loss of microtubules, and they were accompanied by impaired microtubule dynamics and actomyosin hypercontractility. Angiogenic sprouts formed but retracted in SUN1-depleted endothelial cells, and vessels of zebrafish lacking SUN1 had abnormal extension and were defective in forming connections. Thus, endothelial SUN1 regulates peripheral cell-cell junctions from the nucleus, likely via microtubule-based interactions, and this long-range regulation is important for blood vessel formation and barrier function.

Keywords: Endothelial cell, SUN1, LINC, nucleus, junctions, angiogenesis, microtubules, contractility

bioRxiv preprint doi: https://doi.org/10.1101/2021.08.11.455980; this version posted August 11, 2021. The copyright holder for this preprint (which was not certified by peer review) is the author/funder, who has granted bioRxiv a license to display the preprint in perpetuity. It is made available under aCC-BY-NC-ND 4.0 International license.

INTRODUCTION

Blood vessels form and expand via sprouting angiogenesis, a dynamic process whereby endothelial cells migrate from pre-existing vessels to form new conduits (Carmeliet et al. 2011; Bautch et al. 2015; Kushner et al. 2013). During angiogenesis, endothelial cell-cell junctions destabilize and rearrange to allow for repolarization and migration towards pro-angiogenic cues (Dejana 2004; Esser et al. 1998; Blum et al. 2008). As vessels mature, endothelial cell junctions stabilize and form a functional barrier that regulates egress of fluid and oxygen; barrier dysfunction leads to leak and severe disease (Dejana 2004; Rho et al. 2017). Thus, the regulation of endothelial cell junctions is important developmentally and for vascular homeostasis.

Adherens junctions are a key cellular regulatory node of both external and internal inputs, and they coordinate internal input from both the actin and microtubule cytoskeletons. A main component of endothelial cell adherens junctions is VE-cadherin, a protein that forms homodimers via N-terminal interactions with molecules on neighboring cells, and interacts on the cytoplasmic side with α, β, and p120 catenins to link to the actin cytoskeleton (Abu Taha et al. 2014; Dejana et al. 2013). Changes in the actin cytoskeleton affect endothelial cell junctions; for example, increased actomyosin contractility activates and destabilizes endothelial cell adherens junctions (Huveneers et al. 2012; Angulo-Urarte et al. 2018). In contrast, microtubules tether to and affect the function of adherens junctions through less well characterized mechanisms (Stehbens et al. 2009). In endothelial cells, loss of VE-cadherin alters microtubule dynamics, and disruption of microtubule dynamics destabilizes junctions and barrier function (Komarova et al. 2012). Coordination of inputs from the actin and microtubule cytoskeletons regulates endothelial cell permeability via RhoA and RapGTPases

bioRxiv preprint doi: https://doi.org/10.1101/2021.08.11.455980; this version posted August 11, 2021. The copyright holder for this preprint (which was not certified by peer review) is the author/funder, who has granted bioRxiv a license to display the preprint in perpetuity. It is made available under aCC-BY-NC-ND 4.0 International license.

(Sehrawat et al. 2008; Sehrawat et al. 2011; Birukova et al. 2006), but how the inputs are integrated is poorly understood.

The nucleus is usually found far from the cell periphery and junctions, yet it is important for non-transcriptional functions critical to angiogenesis and vascular remodeling, such as establishment of polarity, migration, and mechanotransduction (Guilluy et al. 2014; Tkachenko et al. 2013; Graham et al. 2018). The linker of the nucleoskeleton and cytoskeleton (LINC) complex is comprised of both SUN (Sad1p, UNC-84) and KASH (Klarsicht, ANC-1, Syne/Nesprin Homology) proteins (Starr et al. 2010) that function as a bridge between the nucleus and the cytoskeleton. KASH proteins, also called nesprins, are long spectrin-rich structures that localize to the outer nuclear envelope and interact with actin, microtubules, and intermediate filaments with their N-termini and with SUN proteins in the inner nuclear membrane via their C-termini (Stewart-Hutchinson et al. 2008; Padmakumar et al. 2005; McGee et al. 2006; Starr et al. 2010; Ketema et al. 2007). SUN proteins also interact with lamins in the nuclear envelope (Haque et al. 2006), providing a structural link from the nuclear cortex to the cellular cytoskeleton. In mammals, two SUN proteins are ubiquitously expressed: it is thought that SUN1 preferentially forms complexes with microtubules while SUN2 preferentially forms complexes with actin (Zhu et al. 2017), although both SUNs bind nesprins that biochemically interact with both actin and microtubules (Stewart-Hutchinson et al. 2008; Ostlund et al. 2009), so how complexes are assembled and sorted in cells is unclear.

Genetic deletion experiments demonstrate a requirement for the LINC complex in nuclear positioning *in vivo*. While global loss of either *Sun* gene does not produce

bioRxiv preprint doi: https://doi.org/10.1101/2021.08.11.455980; this version posted August 11, 2021. The copyright holder for this preprint (which was not certified by peer review) is the author/funder, who has granted bioRxiv a license to display the preprint in perpetuity. It is made available under aCC-BY-NC-ND 4.0 International license.

severe developmental defects, loss of both genes is embryonic lethal due to severe nervous system defects downstream of impaired neuronal nuclear migration (Lei et al. 2009; Zhang et al. 2009), and global *Sun2* loss changes nuclear positioning and cell adhesion in the skin, leading to alopecia (Stewart et al. 2015). Cell culture studies reveal that the LINC complex functions in endothelial cells. Loss of nesprin-3 disrupts intermediate filaments and endothelial cell flow responses (Morgan et al. 2011), while disruption of the LINC complex via nesprin-1 or nesprin-2 depletion or via a dominant negative KASH reduces endothelial cell migration, matrix adhesion, and junction properties *in vitro* (King et al. 2014; Denis et al. 2021). However, it is unclear whether the LINC complex functions in the vasculature *in vivo*.

Mutations in the nuclear envelope gene *LMNA* (lamin A/C) cause a premature aging syndrome linked to cardiovascular defects (Capell et al. 2006), and the LINC complex protein SUN1 is mis-expressed in this disease (Chen et al. 2012). Here, we examined how SUN1 functions in blood vessels. We found that endothelial loss of *Sun1* disrupts blood vessel sprouting *in vivo*, and the sprouting defects are associated with abnormal endothelial adherens junctions. In SUN1-depleted endothelial cells, destabilized adherens junctions are downstream of defects in microtubule function that likely increase actomyosin contractility and disrupt junction properties, angiogenic sprouting, and barrier function. Thus, nuclear SUN1 that resides far from endothelial cell junctions regulates endothelial cell-cell communication and functionally relevant cell behaviors.

bioRxiv preprint doi: https://doi.org/10.1101/2021.08.11.455980; this version posted August 11, 2021. The copyright holder for this preprint (which was not certified by peer review) is the author/funder, who has granted bioRxiv a license to display the preprint in perpetuity. It is made available under aCC-BY-NC-ND 4.0 International license.

RESULTS

The nuclear LINC protein SUN1 regulates vascular development

The LINC complex is important for cell migration and polarity (Schneider et al. 2011; Chancellor et al. 2010; Chang et al. 2015), and blood vessel formation involves extensive migration of endothelial cells; thus, we hypothesized that the LINC complex regulates angiogenic sprouting of endothelial cells. Because mutations in endothelial cell *LMNA* associated with human cardiovascular disease are associated with expression changes in the LINC protein SUN1 (Chen et al. 2012), we examined the function of SUN1 in endothelial cells. We first asked whether SUN1 is required *in vivo* for vascular development, utilizing a mouse line carrying a conditional *Sun1* allele that we generated from *Sun1*^{tm1a} "knockout first" mice **(Fig S1a-b)**. *Sun1*$^{fl/fl}$ mice were bred to *Sun1*$^{fl/+}$*;Cdh5CreERT2/+* mice to generate *Sun1*^{iECKO} mice with both endothelial-specific and temporal control over *Sun1* excision, along with littermate controls lacking the excision driver or the floxed *Sun1* allele.

We injected mice with tamoxifen at P1, P2, and P3 to induce excision, and harvested retinas at P7 **(Fig 1a)**. The vasculature of *Sun1*^{iECKO} mice had significantly reduced radial expansion relative to littermate controls **(Fig 1b, d)**, consistent with a role for *Sun1* in vascular development. *Sun1*^{iECKO} retinas also had increased vascular density at the front, suggesting that aberrant endothelial cell migration may be upstream of reduced radial expansion **(Fig 1c, e)**. The vascular phenotype of the mutant mice also suggested that endothelial cell-cell junctions were affected by loss of *Sun1*. We examined the localization of the adherens junction protein VE-cadherin and found that VE-cadherin in *Sun1*^{iECKO} vessels was less linear and more punctate than in controls, consistent with elevated adherens junction turnover and junction instability **(Fig 1f)**.

bioRxiv preprint doi: https://doi.org/10.1101/2021.08.11.455980; this version posted August 11, 2021. The copyright holder for this preprint (which was not certified by peer review) is the author/funder, who has granted bioRxiv a license to display the preprint in perpetuity. It is made available under aCC-BY-NC-ND 4.0 International license.

Together, these data indicate that SUN1 regulates vascular development and endothelial cell-cell junctions *in vivo*.

SUN1 stabilizes endothelial cell-cell junctions and regulates barrier function

The pattern of VE-cadherin staining in the vessels of *Sun1*^{iECKO} mice led us to examine more rigorously the hypothesis that SUN1 is necessary for proper endothelial cell adherens junction morphology. To this end, we reduced levels of SUN1 in endothelial cells via siRNA knockdown (KD) **(Fig S2a-c)**. Primary human umbilical vein endothelial cells (HUVEC) with SUN1 KD had more serrated cell-cell junctions, indicative of activated and destabilized junctions in confluent monolayers **(Fig 2a)**. Reduced levels of SUN1 were not associated with altered cell proliferation, as EdU labeling and Ki67 staining revealed no significant difference in either parameter relative to controls treated with non-targeting siRNA (NT) **(Fig S2d-g)**. Since activated and destabilized endothelial cell adherens junctions are associated with impaired barrier function, we measured electrical resistance across endothelial monolayers using Real Time Cell Analysis (RTCA) that provides an impedance value that positively correlates with barrier function. We found that SUN1 KD endothelial cells had reduced electrical resistance compared to controls **(Fig 2b-c)**, consistent with the activated junction morphology and indicative of impaired barrier function. We also assessed the status of junctions in SUN1 KD endothelial cells at confluence using a biotin labeling assay (Dubrovskyi et al. 2013) and found a significant increase in the fluorescent signal in SUN1 KD monolayers **(Fig S3a-b)**, consistent with the impedance data and indicating that loss of SUN1 destabilizes cell-cell junctions. These data support the hypothesis that nuclear SUN1 is required for proper endothelial cell junction morphology and function.

bioRxiv preprint doi: https://doi.org/10.1101/2021.08.11.455980; this version posted August 11, 2021. The copyright holder for this preprint (which was not certified by peer review) is the author/funder, who has granted bioRxiv a license to display the preprint in perpetuity. It is made available under aCC-BY-NC-ND 4.0 International license.

Over-activated cell-cell junctions can result from abnormal junction formation or the inability of formed junctions to stabilize. To determine whether endothelial cell junction formation and stabilization in real time depends on SUN1 function, we disassembled calcium-dependent endothelial cell-cell junctions using the calcium-chelator EDTA, then did a washout to allow for junction reformation. Junction morphology was measured using line scans of VE-cadherin intensity along the cell-cell junctions **(Fig S3c)**, such that junctions with a linear VE-cadherin signal had a higher value than those with more serrated patterns. At 20 min post-washout, no significant difference between SUN1 KD and control junctions was seen via VE-cadherin staining, indicating that SUN1 does not affect endothelial adherens junction formation **(Fig 2d-e)**. However, by 40 min post-washout, a significant increase in serrated junctions and gaps between endothelial cells in SUN1 KD cells was seen relative to controls, and this trend became more pronounced at 60 min post-washout **(Fig 2d-e)**. Consistent with these findings, SUN1 KD endothelial cells also had increased VE-cadherin internalization at steady state, which is consistent with actively remodeling junctions **(Fig 2f-g)**. Thus, SUN1 is not required to form endothelial cell-cell junctions, but it is necessary for proper junction maturation and stabilization.

SUN1 regulates endothelial cell contractility

Cellular changes in actomyosin contractility contribute to activation of cell-cell junctions (Huveneers et al. 2012; Rauzi et al. 2010), and loss of SUN1 leads to a SUN2-dependent increase in RhoA activity in HeLa cells (Thakar et al. 2017). Since RhoA is an important effector of actomyosin dynamics and contractility, we hypothesized that activated cell-cell junctions following SUN1 KD were downstream of elevated actomyosin contractility. SUN1 KD endothelial cells had reduced cortical actin, more

bioRxiv preprint doi: https://doi.org/10.1101/2021.08.11.455980; this version posted August 11, 2021. The copyright holder for this preprint (which was not certified by peer review) is the author/funder, who has granted bioRxiv a license to display the preprint in perpetuity. It is made available under aCC-BY-NC-ND 4.0 International license.

radial actin bundles at the periphery, and increased phosphorylated myosin light chain (ppMLC), consistent with increased actomyosin contractility **(Fig S4a-b)**. To further test the role of SUN1 in actomyosin contractility, we blocked myosin-II ATPase activity or Rho kinase (ROCK) pharmacologically with blebbistatin or Y-27632, respectively, and found that each treatment rescued the over-activated cell-cell junctions seen with reduced SUN1 levels in endothelial cells **(Fig 3a-d)**. Blockade of myosin-II or ROCK also rescued the radial actin structures seen in SUN1 KD endothelial cells **(Fig S4c-d)**. In contrast, treatment with an inducer of actomyosin contractility, thrombin, phenocopied SUN1 KD with over-activated junctions in control endothelial cells and did not further activate the junctions of SUN1 KD endothelial cells, suggesting that SUN1 loss induces a maximal contractile state in endothelial cells **(Fig 3e-f)**.

Because SUN2 is associated with regulation of the actin cytoskeleton in non-endothelial cells (Zhu et al. 2017), we asked whether the hypercontractility induced by SUN1 loss was SUN2-dependent by co-depleting both SUN1 and SUN2. Under these conditions, cell-cell junctions were not over-activated despite loss of SUN1, and endothelial cells with both SUN1 and SUN2 reduced did not respond to thrombin with junction overactivation **(Fig 3e-f)**, revealing that hypercontractility following SUN1 KD is SUN2-dependent. Taken together, these data indicate that loss of SUN1 results in SUN2-dependent actomyosin hypercontractility and over-activated cell-cell junctions in endothelial cells.

SUN1 regulates microtubule localization and dynamics in endothelial cells

SUN1 is thought to preferentially form LINC complexes with the microtubule cytoskeleton (Zhu et al. 2017), and microtubule dynamics regulate endothelial cell-cell

bioRxiv preprint doi: https://doi.org/10.1101/2021.08.11.455980; this version posted August 11, 2021. The copyright holder for this preprint (which was not certified by peer review) is the author/funder, who has granted bioRxiv a license to display the preprint in perpetuity. It is made available under aCC-BY-NC-ND 4.0 International license.

junctions (Komarova et al. 2012; Sehrawat et al. 2008; Sehrawat et al. 2011). Microtubule dynamics also directly influence actomyosin contractility; microtubule depolymerization leads to the release of GEF-H1 to activate RhoA and induce actomyosin contractility, resulting in endothelial barrier dysfunction (Verin et al. 2001; Birukova et al. 2006). Thus, we asked whether the observed adherens junction defects following SUN1 depletion resulted from changes in the microtubule cytoskeleton. We found that microtubule depolymerization using nocodazole treatment phenocopied SUN1 KD and led to destabilized adherens junctions in control endothelial cells, but loss of microtubules did not exacerbate the cell-cell junction defects seen with SUN1 KD **(Fig 4a-b)**. Interestingly, endothelial cells reduced for both SUN1 and SUN2 were resistant to the effects of microtubule depolymerization on junctions **(Fig 4a-b)**. These findings indicate that altered microtubule dynamics affect endothelial cell junctions, and this effect requires SUN2 function.

We next asked whether SUN1 was required for proper microtubule localization via staining for α-tubulin. We found that α-tubulin levels around the MTOC were not affected by reduced levels of SUN1 or SUN1 and SUN2 (SUN1/2) **(Fig S5a)**; however, significantly fewer microtubules reached the cell periphery and cell-cell junctions in SUN1 KD endothelial cells compared to controls or SUN1/2 double KD (dKD) cells **(Fig 4c-e)**. Significantly fewer microtubules were found surrounding the nucleus in SUN1 KD and SUN1/2 dKD endothelial cells **(Fig 4c-e)**, suggesting that both peripheral and nuclear microtubule localization is SUN1-dependent, while peripheral microtubule localization is also SUN2-dependent. To test whether changes in microtubule localization were associated with altered microtubule dynamics, we performed microtubule TIP tracking via labeling with the TIP protein EB3. This analysis revealed

bioRxiv preprint doi: https://doi.org/10.1101/2021.08.11.455980; this version posted August 11, 2021. The copyright holder for this preprint (which was not certified by peer review) is the author/funder, who has granted bioRxiv a license to display the preprint in perpetuity. It is made available under aCC-BY-NC-ND 4.0 International license.

that SUN1 KD or SUN1/2 dKD led to reduced microtubule comet velocity, lifetime, and displacement, consistent with microtubule dynamics being impaired downstream of loss of SUN1 **(Fig S5b-d)**. Taken together, these results show that endothelial SUN1 regulates microtubule localization and dynamics, and that microtubule changes with SUN1 KD prevent microtubules from reaching the cell periphery when SUN2 is present, suggesting that cytoskeletal changes with SUN1 depletion lead to activated cell-cell junctions.

Nuclear SUN1 is required for sprouting angiogenesis

Regulation of the endothelial cell cytoskeleton and adherens junctions is crucial for angiogenesis (Angulo-Urarte et al. 2018; Wylie et al. 2018). *Sun1* loss affects vascular development in the postnatal mouse retina **(Fig 1)**, but this tissue is not amenable to live imaging over long time periods. To query dynamic aspects of angiogenic sprouting, we first utilized a 3D sprouting model coupled with temporal image acquisition (Nakatsu et al. 2008). Examination of vessels fixed after 7 days of sprouting revealed that reduced SUN1 levels led to a significant decrease in angiogenic sprout length and branching **(Fig 5a-c)**, reminiscent of the decreased radial expansion seen in the $Sun1^{iECKO}$ vessels of the mouse retina **(Fig 1d)**. Live-cell imaging revealed that control sprouts typically elongated over time, with very few sprouts retracting once they moved out from the bead **(Fig 5d-e, Movie S1)**. In contrast, SUN1 KD structures had significantly increased numbers of retracting sprouts, and many sprouts collapsed partially or completely **(Fig 5d-e, Movie S2)**. These data show that SUN1 is required for proper vascular sprout morphology, and reduced sprout length and branching are likely downstream of excess sprout retractions in vessels with depleted SUN1.

bioRxiv preprint doi: https://doi.org/10.1101/2021.08.11.455980; this version posted August 11, 2021. The copyright holder for this preprint (which was not certified by peer review) is the author/funder, who has granted bioRxiv a license to display the preprint in perpetuity. It is made available under aCC-BY-NC-ND 4.0 International license.

We next analyzed how Sun1 manipulations affect sprouting angiogenesis in embryonic zebrafish using a *Tg(fli:LifeAct-GFP)* reporter line that labels the actin cytoskeleton of endothelial cells; this approach allowed for live image analysis in a model that includes blood flow as vessels develop. Zebrafish have two *Sun1* genes, *Sun1a* and *Sun1b*; however, the SUN domain of *Sun1b* is more homologous to human *Sun1,* and Sun1b is more highly expressed in cardiovascular tissue, so this gene was chosen for manipulation using two strategies. We depleted Sun1b in zebrafish embryos via morpholino injection (MO) at the 1-cell stage, and we also analyzed fish carrying a point mutation in the *Sun1b* gene leading to a premature stop codon, referred to as *Sun1b*$^{sa33109/sa33109}$ (see Methods for details). Loss of *Sun1b* led to an increase in ectopic endothelial cell sprouting in and around the inter-segmental vessels (ISV) of both morphant and mutant fish at 24 hpf **(Fig 6a-b)**. At 33-34 hpf, Sun1b morphants had significantly increased numbers of endothelial cell filopodia, and these filipodia were shorter than controls, in the ISVs that sprouted towards and connected to the dorsal longitudinal anastomotic vessel (DLAV) **(Fig 6c-d)**; these numbers trended in the same direction in *Sun1b* mutants **(Fig 6f-h)**. These changes are consistent with over-activated endothelial cells following Sun1b depletion in zebrafish.

To examine dynamic changes in vascular sprouting downstream of Sun1b manipulations *in vivo*, Sun1b morphant fish were imaged from 26-36 hpf. In control fish, the ISVs sprouted towards the dorsal plane and connected to the DLAV between 32-36 hpf **(Fig 6i-j, Movie S3)**. In contrast, numerous ISVs either failed to reach the DLAV or made aberrant connections in Sun1b morphant fish **(Fig 6i-j, Movie S4)**. These results complement the 3D sprouting analysis and show that the nuclear LINC complex protein SUN1 is crucial to regulation of endothelial cell sprouting dynamics *in vivo*.

bioRxiv preprint doi: https://doi.org/10.1101/2021.08.11.455980; this version posted August 11, 2021. The copyright holder for this preprint (which was not certified by peer review) is the author/funder, who has granted bioRxiv a license to display the preprint in perpetuity. It is made available under aCC-BY-NC-ND 4.0 International license.

DISCUSSION

The nucleus compartmentalizes and organizes genetic material, but how the nucleus communicates with other organelles and the cytoskeleton to regulate cell behaviors during interphase is poorly understood. Here, we show for the first time that the nuclear LINC complex protein SUN1 regulates endothelial cell-cell junctions, and that this regulation goes through the microtubule cytoskeleton to affect both microtubule and actin dynamics. Our data is consistent with a model in which abnormal microtubule dynamics contribute to increased actomyosin contractility downstream of SUN1 depletion, blocking already fragile microtubules from reaching the cell periphery **(Fig 6k)**. The combination of actomyosin hypercontractility and reduced peripheral microtubules leads to destabilization of endothelial cell adherens junctions that impairs blood vessel formation in fish and mice. Thus, SUN1 is a critical regulator of communication between the endothelial cell nucleus and the cell periphery.

Our findings reveal that the LINC complex protein SUN1 is required for endothelial adherens junction stabilization and proper blood vessel formation. The adherens junctions of expanding retinal vessels appear destabilized in mice lacking endothelial *Sun1*, and this cellular phenotype is accompanied by reduced radial expansion and increased density of the network, suggesting that destabilized junctions contribute to the vessel network perturbations. Mutations in other genes that affect endothelial cell junction integrity, such as *Smad6*, *Pi3kca*, and *Yap/Taz*, also perturb angiogenesis in the retina (Wylie et al. 2018; Angulo-Urarte et al. 2018; Neto et al. 2018). Live imaging of active vessel sprouting in the zebrafish showed that Sun1 loss led to changes in filopodia characteristics, ectopic sprouting, and defective anastomosis, which is consistent with our finding that mammalian endothelial cell

bioRxiv preprint doi: https://doi.org/10.1101/2021.08.11.455980; this version posted August 11, 2021. The copyright holder for this preprint (which was not certified by peer review) is the author/funder, who has granted bioRxiv a license to display the preprint in perpetuity. It is made available under aCC-BY-NC-ND 4.0 International license.

sprouts with SUN1 depletion retract more often that controls. Altered sprout dynamics are also found in situations where VE-cadherin is absent or abnormal such as Wnt inhibition, loss of VE-cadherin, PI3-kinase inhibition, and excess centrosomes (Hübner et al. 2018; Sauteur et al. 2017; Sauteur et al. 2014; Kushner et al. 2016; Buglak et al. 2020; Angulo-Urarte et al. 2018). However, until now, angiogenic sprouting defects have not been associated with mutations that affect the LINC complex and/or SUN1. Unlike genes encoding components of junctions and signaling effectors, SUN1 functions at significant cellular distances from cell junctions.

How does SUN1 regulate endothelial cell-cell junctions from a distance? SUN1 is thought to be important in microtubule-associated LINC complexes (Zhu et al. 2017), and disruption of microtubules or their dynamics destabilizes adherens junctions in both endothelial and non-endothelial cells (Komarova et al. 2012; Stehbens et al. 2006; Vasileva et al. 2018). Our data show that SUN1 depletion is sufficient to impair both microtubule dynamics and microtubule localization. Microtubule TIP tracking parameters revealed decreased extension velocity, growth lifetime, and displacement, while localization revealed that SUN1 loss led to significantly less microtubule density at the cell periphery. The effects of SUN1 depletion in destabilizing endothelial cell junctions were phenocopied by microtubule depolymerization, suggesting that altered microtubule dynamics and localization downstream of reduced SUN1 levels leads to endothelial cell junction defects.

Interestingly, depletion of both SUN1 and SUN2 did not prevent microtubules from reaching the cell periphery, despite leading to abnormal microtubule dynamics and preventing nuclear localization. Furthermore, cells lacking both SUN1 and SUN2 were

bioRxiv preprint doi: https://doi.org/10.1101/2021.08.11.455980; this version posted August 11, 2021. The copyright holder for this preprint (which was not certified by peer review) is the author/funder, who has granted bioRxiv a license to display the preprint in perpetuity. It is made available under aCC-BY-NC-ND 4.0 International license.

resistant to both nocodazole and thrombin-induced changes to endothelial adherens junctions, indicating that a SUN2-dependent process also contributes to the overall outcome of SUN1 depletion on junctions. We identified a SUN2-dependent increase in actomyosin contractility following SUN1 depletion in endothelial cells. Consistent with the finding that HeLa cells have a SUN2-dependent increase in RhoA activity with SUN1 KD (Thakar et al. 2017), increased endothelial cell contractility with SUN1 depletion is linked to elevated RhoA activity, as inhibition of Rho-kinase (ROCK) rescued the SUN1 depletion-induced destabilization of endothelial junctions.

Microtubules regulate Rho signaling via sequestration of the Rho-specific exchange factor GEF-H1; microtubule depolymerization releases GEF-H1 to activate RhoA signaling, elevate actomyosin contractility, and impair barrier function in endothelial cells (Verin et al. 2001; Birukova et al. 2004; Birukova et al. 2006). Thus, altered microtubule dynamics downstream of SUN1 depletion may lead directly to elevated RhoA activity and SUN2-dependent actomyosin hypercontractility that in turn affects microtubule organization and function at the cell periphery. Moreover, a retrograde actin polymerization gradient intersects with microtubules extending towards the periphery (Waterman-Storer et al. 1999; Wittmann et al. 2003), and disrupted microtubule function downstream of centrosome abnormalities in endothelial cells prevents microtubules from reaching the periphery and disturbs adherens junctions (Kushner et al. 2016; Buglak et al. 2020). SUN1 depletion-induced actomyosin hypercontractility led to increased radial actin bundles at the cell periphery, suggesting that destabilized junctions result from a combination of SUN1-instigated changes in microtubule dynamics and increased actomyosin activity, leading to hypercontractility that blocks fragile microtubules from reaching adherens junctions.

bioRxiv preprint doi: https://doi.org/10.1101/2021.08.11.455980; this version posted August 11, 2021. The copyright holder for this preprint (which was not certified by peer review) is the author/funder, who has granted bioRxiv a license to display the preprint in perpetuity. It is made available under aCC-BY-NC-ND 4.0 International license.

Our finding that SUN1 regulates endothelial cell junctions and blood vessel expansion has implications for diseases associated with aging, as vascular defects underlie most cardiovascular disease. Children with Hutchinson-Gilford Progeria Syndrome (HGPS) have a mutation in the *LMNA* gene encoding lamin A/C that results in accumulation of a an incompletely processed lamin protein called progerin; these patients age rapidly and die in their early to mid-teens from severe atherosclerosis (De Sandre-Giovannoli 2003; Eriksson et al. 2003; Olive et al. 2010). Progerin has increased affinity for SUN1 that leads to accumulation of SUN1 in HGPS patient cells (Chen et al. 2012; Chang et al. 2019; Chen et al. 2014; Haque et al. 2010). Loss of *Sun1* partially rescues progeria phenotypes in mouse models and patient cells (Chen et al. 2012; Chang et al. 2019), and endothelial cells have increased SUN1 accumulation in HGPS mouse models (Osmanagic-Myers et al. 2019). Thus, nuclear membrane perturbations affecting SUN1 cause disease, and here we find that nuclear SUN1 links through microtubules to affect both the microtubule and actin cytoskeletons. These effects are transmitted to endothelial cell-cell junctions far from the site of SUN1 localization to influence endothelial cell behaviors and blood vessel sprouting.

bioRxiv preprint doi: https://doi.org/10.1101/2021.08.11.455980; this version posted August 11, 2021. The copyright holder for this preprint (which was not certified by peer review) is the author/funder, who has granted bioRxiv a license to display the preprint in perpetuity. It is made available under aCC-BY-NC-ND 4.0 International license.

MATERIALS & METHODS

Microscopy

Unless otherwise stated, all imaging was performed as follows: confocal images were acquired with an Olympus confocal laser scanning microscope and camera (Fluoview FV3000, IX83) using a UPlanSApo 40x silicone-immersion objective (NA 1.25), UPlanSApo 60x oil-immersion objective (NA 1.40), or UPlanSApo 100x oil-immersion objective (NA 1.40). Imaging was performed at RT for fixed samples. Images were acquired with the Olympus Fluoview FV31S-SW software and all image analysis, including Z-stack compression, was performed in Fiji (Schindelin et al. 2012; Linkert et al. 2010). Any adjustments to brightness and contrast were performed evenly for images in an experiment.

Mice

All experiments involving animals were performed with approval from the University of North Carolina, Chapel Hill Institutional Animal Care and Use Committee (IACUC). C57Bl6N-*Sun1*$^{tm1a(EUCOMM)Wtsi}$/CipheOrl mice were obtained from the European Mouse Mutant Archive (EMMA) mouse repository. FlpO-B6N-Albino (Rosa26-FlpO/+) mice were obtained from the UNC Animal Models Core. *Tg(Cdh5-cre/ERT2)1Rha* mice were generated by Dr. Ralf Adams (Sörensen et al. 2009) and obtained from Cancer Research UK. The *Sun1*^{tm1a} allele was identified via genomic PCR to amplify the LacZ insertion (Forward: 5’- ACTATCCCGACCGCCTTACT-3’; Reverse: 5’-TAGCGGCTGATGTTGAACTG-3’). The *Sun1*^{fl} allele was generated by breeding *Sun1*^{tm1a} mice with FlpO-B6N-Albino (Rosa26-FlpO/+) mice to excise the *lacZ* insertion. The *Sun1*^{fl} allele was identified via genomic PCR using the following primers (Forward: 5’- GCTCTCTGAAACATGGCTGA-3’; Reverse: 5’- ATCCGGGGTGTTTGGATTAT-3’).

bioRxiv preprint doi: https://doi.org/10.1101/2021.08.11.455980; this version posted August 11, 2021. The copyright holder for this preprint (which was not certified by peer review) is the author/funder, who has granted bioRxiv a license to display the preprint in perpetuity. It is made available under aCC-BY-NC-ND 4.0 International license.

*Sun1^fl^* mice were bred to *Tg(Cdh5-cre/ERT2)1Rha* mice to generate *Sun1^fl/fl^;Cdh5CreERT2* pups for endothelial-selective and temporally controlled deletion of exon 4 of the *Sun1* gene. PCR genotyping for FlpO and Cdh5CreERT2 mice was performed with the following primers (FlpO: Forward: 5'-TGAGCTTCGACATCGTGAAC -3'; Reverse: 5'-TCAGCATCTTCTTGCTGTGG-3') (Cdh5CreERT2: Forward: 5'-TCCTGATGGTGCCTATCCTC-3'; Reverse: 5'- CCTGTTTTGCACGTTCACCG-3'). Induction of Cre was performed via IP injection of pups at P1, P2, and P3 with 50μl of 1mg/ml tamoxifen (T5648, Sigma) dissolved in sunflower seed oil (S5007, Sigma). Littermates lacking either *Cdh5CreERT2* or the *Sun1^fl^* allele were used as controls.

Mouse retinas

Tamoxifen-injected mice were sacrificed at P7, eyes were collected, fixed in 4% PFA for 1h at RT, then dissected and stored at 4°C in PBS for up to 2 weeks (Chong et al. 2017). Retinas were permeabilized in 0.5% Triton X-100 (T8787, Sigma) for 1h at RT, blocked for 1h at RT in blocking solution (0.3% Triton X-100, 0.2% BSA (A4503, Sigma), and 5% goat serum (005-000-121, Jackson Immuno)), then incubated with VE-cadherin antibody (anti-mouseCD144, 1:100, 550548, BD Pharmingen) in blocking solution overnight at 4°C. Samples were washed 3X, then incubated with Isolectin B4 AlexaFluor 488 (1:100, I21411, ThermoFisher) and goat anti-rat AlexaFluor 647 (1:500, A21247, Life Technologies) for 1h at RT. Retinas were mounted with Prolong Diamond Antifade mounting medium (P36961, Life Technology) and sealed with nail polish. Images were obtained using either a UPlanSApo 10x air objective (NA 0.40) or UPlanSApo 40x silicone-immersion objective (NA 1.25). Percent radial expansion was calculated by dividing the distance from the retina center to the vascular front by the distance from the retina center to the edge of the tissue. Four measurements/retina

bioRxiv preprint doi: https://doi.org/10.1101/2021.08.11.455980; this version posted August 11, 2021. The copyright holder for this preprint (which was not certified by peer review) is the author/funder, who has granted bioRxiv a license to display the preprint in perpetuity. It is made available under aCC-BY-NC-ND 4.0 International license.

were averaged. Vascular density was measured by imaging a 350μm x 350μm ROI at the vascular edge. Fiji was used to threshold images, and the vessel area was normalized to the area of the ROI (n=4 ROI/retina, chosen at 2 arteries and 2 veins).

Cell culture

HUVEC (C2519A, Lonza) were cultured in EBM-2 (CC-3162, Lonza) supplemented with the Endothelial Growth Medium (EGM-2) bullet kit (CC-3162, Lonza) and 1x antibiotic-antimycotic (Gibco). Normal human lung fibroblasts (CC2512, Lonza) were cultured in DMEM (Gibco) with 10% fetal bovine serum (FBS) and 1x antibiotic-antimycotic (Gibco). All cells were maintained at 37°C and 5% CO_2. For contractility inhibition experiments, HUVEC were treated with 10μM (-)Blebbistatin (B0560-1MG, Sigma) for 15 min at 37°C or 10μM Y-27632 (10187-694, VWR) for 30 min at 37°C then immediately fixed in 4% PFA. For induction of contractility, HUVEC were treated with 0.5U/ml thrombin (T7201-500UN, Sigma) for 10 min at 37°C. For microtubule depolymerization, HUVEC were treated with 10μM nocodazole (M1404, Sigma) for 20 min at 37°C then immediately fixed in methanol.

siRNA knockdown

HUVEC were transfected with non-targeting siRNA (NT, #4390847, Life Technologies), SUN1 siRNA (439240, #s23630, Life Technologies), and/or SUN2 siRNA (439240, #s24467, Life Technologies) using Lipofectamine 2000 (11668027, Invitrogen) or Lipofectamine 3000 (L3000015, ThermoFisher). siRNA at 0.48μM in Opti-MEM (31985-070, Gibco) and a 1:20 dilution of Lipofectamine in Opti-MEM were incubated separately at RT for 5 min, then combined and incubated at RT for 15 min. HUVEC were transfected at ~80% confluency with siRNA at 37°C for 24h, then

bioRxiv preprint doi: https://doi.org/10.1101/2021.08.11.455980; this version posted August 11, 2021. The copyright holder for this preprint (which was not certified by peer review) is the author/funder, who has granted bioRxiv a license to display the preprint in perpetuity. It is made available under aCC-BY-NC-ND 4.0 International license.

recovered in EGM-2 for an additional 24h. HUVEC were seeded onto glass chamber slides coated with 5μg/ml fibronectin (F2006-2MG, Sigma) for experiments.

Immunofluorescence staining

For experiments visualizing microtubules, HUVEC were fixed in ice-cold methanol for 10 min at 4°C. For all other experiments, HUVEC were fixed with 4% PFA for 10 min at RT and permeabilized with 0.1% Triton X-100 (T8787, Sigma) for 10 min at RT. Fixed HUVEC were blocked for 1h at RT in blocking solution (5% FBS, 2X antibiotic-antimycotic (Gibco), 0.1% sodium azide (s2002-100G, Sigma) in DPBS). Cells were incubated in primary antibody overnight at 4°C, then washed 3X for 5 min in DPBS. Secondary antibody and DRAQ7 (1:1000, ab109202, Abcam), DAPI (0.3μM, 10236276001, Sigma), and/or AlexaFluor488 Phalloidin (1:100, A12379, Life Technologies) were added for 1h at RT followed by 3X washes for 10 min each in DPBS. Slides were mounted with coverslips using Prolong Diamond Antifade mounting medium (P36961, Life Technology) and sealed with nail polish. Primary and secondary antibodies were diluted in blocking solution. The following primary antibodies were used: anti-VE-cadherin (1:500, 2500S, Cell Signaling), anti-SUN1 (1:500, ab124770, Abcam), anti-SUN2 (1:1000, MABT880, Sigma), anti-Ki67 (1:500, ab15580, Abcam), anti-phospho-myosin light chain 2 (Thr18/Ser19) (1:500, 3674S, Cell Signaling), and anti-alpha-tubulin (1:500, 3873S, Cell Signaling). The following secondary antibodies from Life Technologies were used: goat anti-mouse AlexaFluor 488 (1:500, A11029) and goat anti-rabbit AlexaFluor 594 (1:500, A11037).

bioRxiv preprint doi: https://doi.org/10.1101/2021.08.11.455980; this version posted August 11, 2021. The copyright holder for this preprint (which was not certified by peer review) is the author/funder, who has granted bioRxiv a license to display the preprint in perpetuity. It is made available under aCC-BY-NC-ND 4.0 International license.

EdU labeling

HUVEC were labeled with EdU using the Click-It EdU Kit 488 (Invitrogen, C10337) and fixed according to the manufacturer's instructions. Cells positive for EdU labeling were counted and compared to total cell number to obtain percent positive.

Junction analysis

Endothelial cell adherens junctions were quantified in monolayers using Fiji to generate 15μm line scans of VE-cadherin signal parallel to the cell junctions. VE-cadherin signal was integrated to obtain the area under the curve. Linear junctions with consistent VE-cadherin signal thus had a large area under the curve, while more serrated junctions had reduced area under the curve **(Fig S3c)**. Measurements were performed on at least 9 cells per field of view, with 3-6 fields of view per condition.

Real time cell analysis (RTCA)

Barrier function was assessed using the xCELLigence Real-Time Cell Analyzer (RTCA, Acea Biosciences/Roche Applied Science) to measure electrical impedance across HUVEC monolayers seeded onto microelectrodes. HUVEC were seeded to confluency on the microelectrodes of the E-plate (E-plate 16, Roche Applied Science). Electrical impedance readings were taken every 2 min for 5h. The percent change in cell index was obtained at the 5h timepoint using the following formula: (Cell $Index_{SUN1}$-Cell $Index_{NT}$)/ABS(Cell $Index_{NT}$).

Biotin labeling assay

Barrier function was assessed as described (Dubrovskyi et al. 2013). Briefly, fibronectin was biotinylated by incubating 0.1mg/mL fibronectin with 0.5mM EZ-Link

bioRxiv preprint doi: https://doi.org/10.1101/2021.08.11.455980; this version posted August 11, 2021. The copyright holder for this preprint (which was not certified by peer review) is the author/funder, who has granted bioRxiv a license to display the preprint in perpetuity. It is made available under aCC-BY-NC-ND 4.0 International license.

Sulfo-NHS-LC-Biotin (A39257, ThermoFisher) for 30 min at RT. Glass chamber slides were coated with 5µg/ml biotinylated-fibronectin and HUVEC were seeded on top. At confluency, HUVEC were treated with 25µg/mL Streptavidin-488 (S11223, Invitrogen) for 3 min then immediately fixed. For quantification, Fiji was used to threshold the streptavidin signal, and the streptavidin area was measured and normalized for total area for at least 3 fields of view per experiment.

Junction reformation assay

The EDTA junction reformation assay was performed as previously described (Wright et al. 2015). Briefly, HUVEC were treated with 3mM EDTA (EDS-100G, Sigma-Aldrich) for 1h at 37°C. EDTA was then washed out 3X with DPBS, incubation at 37°C in EGM-2 was continued, and cells were fixed at 0 min, 20 min, 40 min, and 60 min intervals.

VE-cadherin internalization

VE-cadherin internalization was performed as described (Wylie et al. 2018). Briefly, HUVEC were plated on 5µg/ml fibronectin and grown to confluency. After overnight serum starvation (Opti-MEM (31985-070, Gibco) supplemented with 1% FBS (F2442, Sigma), and 1x antibiotic-antimycotic (Gibco)), cells were washed with pre-chilled PBS+ (14040182, ThermoFisher) on ice at 4°C, then incubated in ice-cold blocking solution (EBM-2 (CC-3162, Lonza) supplemented with 0.5% BSA (A4503, Sigma)) for 30 min at 4°C. HUVEC were then incubated with VE-cadherin BV6 antibody (1:100, ALX-803-305-C100, Enzo) in blocking solution for 2h on ice at 4°C. Following VE-cadherin labeling, cells were washed with PBS+ then incubated in pre-warmed internalization medium (EBM-2) at 37°C for 1h. Finally, HUVEC were incubated in acid

bioRxiv preprint doi: https://doi.org/10.1101/2021.08.11.455980; this version posted August 11, 2021. The copyright holder for this preprint (which was not certified by peer review) is the author/funder, who has granted bioRxiv a license to display the preprint in perpetuity. It is made available under aCC-BY-NC-ND 4.0 International license.

wash (0.5M NaCl/0.2M acetic acid) for 4 min at 4°C to remove remaining labeled VE-cadherin on the cell surface, then washed with PBS+ and fixed. For quantification, internalized VE-cadherin area was measured in Fiji, then normalized to total cell area for at least 9 cells per experiment.

Density analysis for α-tubulin

Peripheral microtubule analysis was performed in Fiji as follows: a 4.5μm x 4μm ROI was drawn at the MTOC, the cell periphery, and over the nucleus. Fiji was used to threshold α-tubulin signal, and the area of the signal was measured within the ROI. Peripheral α-tubulin and nuclear α-tubulin signal was then normalized to MTOC α-tubulin signal for each cell. This was performed on 8 cells per field of view, with 3-6 fields per condition per experiment.

Microtubule TIP tracking

HUVEC were infected with an EB3-mCherry Lentivirus (Kushner et al. 2014) for 24h to visualize microtubule comets. Following infection, HUVEC were incubated with siRNAs for NT, SUN1, or SUN1/2. For live imaging, cells were incubated at 37°C in a stage-top incubator (TOKAI HIT, WSKM). Images were acquired every 1.5 sec for 22 sec using a UPlanSApo 100x oil-immersion objective (NA 1.40). Microtubules were tracked using the plus Tip Tracker software program in MATLAB (Jaqaman et al. 2008). Tracking parameters were: maximum gap length of 12 frames; minimum track length of 3 frames, search radium range 5-10 pixels; maximum forward angle of 25°; maximum backward angle of 8°; maximum shrinkage factor of 1.0; and fluctuation radius of 2 pixels.

bioRxiv preprint doi: https://doi.org/10.1101/2021.08.11.455980; this version posted August 11, 2021. The copyright holder for this preprint (which was not certified by peer review) is the author/funder, who has granted bioRxiv a license to display the preprint in perpetuity. It is made available under aCC-BY-NC-ND 4.0 International license.

3D sprouting angiogenesis assay

The 3D sprouting angiogenesis assay was performed as previously described (Nakatsu et al. 2008; Nesmith et al. 2017). 48h following siRNA knockdown, HUVEC were coated onto cytodex 3 microcarrier beads (17048501, GE Healthcare Life Sciences) and embedded in a fibrin matrix by combining 7µl of 50U/ml thrombin (T7201-500UN, Sigma) with 500µl of 2.2 mg/ml fibrinogen (820224, Fisher) in a 24-well glass-bottomed plate (662892, Grenier Bio). The matrix was incubated for 20 min at RT followed by 20 min at 37°C to allow the matrix to solidify. EGM-2 was then added to each well along with 200µl of normal human lung fibroblasts (CC2512, Lonza) at a concentration of $2x10^5$ cells/ml. At day 7 of sprouting, fibroblasts were removed via trypsin treatment (5X-trypsin for 3min at 37°C), and samples were fixed in 4% PFA for 15 min at RT. 0.5% Triton X-100 in DBPS was added to the wells, and incubation was overnight at 4°C. After rinsing 3X in DPBS, samples were blocked (5% goat serum (005-000-121, Jackson Immuno), 1% BSA (A4503, Sigma), and 0.3% Triton X-100 (T8787, Sigma)) overnight at 4°C. Samples were rinsed 3X in DBPS, then DAPI (0.3µM, 10236276001, Sigma) and AlexaFluor488 Phalloidin (1:50, A12379, Life Technologies) in blocking solution were added to the wells, and incubation was overnight at 4°C prior to rinsing 3X in DPBS. Images were acquired in the Z-plane using a UPlanSApo 20x oil-immersion objective (NA 0.58) and processed in Fiji. Average sprout length was measured by tracing each sprout from base (bead) to tip, then averaging lengths per bead. Branching was measured by counting total branch points and normalizing to total sprout length per bead using the AnalyzeSkeleton plugin (Arganda-Carreras et al. 2010).

bioRxiv preprint doi: https://doi.org/10.1101/2021.08.11.455980; this version posted August 11, 2021. The copyright holder for this preprint (which was not certified by peer review) is the author/funder, who has granted bioRxiv a license to display the preprint in perpetuity. It is made available under aCC-BY-NC-ND 4.0 International license.

Live imaging on HUVEC sprouts was performed between days 4-6.5 of sprouting. Images were acquired on an Olympus VivaView Incubator Fluorescence Microscope with a UPLSAPO 20x objective (NA 0.75) and 0.5x magnification changer (final magnification 20x) with a Hamamatsu Orca R2 cooled CCD camera at 30 min intervals for 60h at 37°C. Images were acquired using the MetaMorph imaging software and analyzed in Fiji. Sprouts were considered to have "retracted" if they regressed towards the bead for at least 3 imaging frames (1.5h).

Zebrafish

All experimental Zebrafish (*Danio rerio*) procedures performed in this study were reviewed and approved by the University of North Carolina Chapel Hill Animal Care and Use Committee. Animals were housed in an AAALAC-accredited facility in compliance with the *Guide for the Care and Use of Laboratory Animals* as detailed on protocols.io (dx.doi.org/10.17504/protocols.io.bg3jjykn). *Tg(fli:LifeAct-GFP)* was a gift from Wiebke Herzog. *Sun1b*^{sa33109} mutant fish were obtained from the Zebrafish International Resource Center (ZIRC). For genotyping, the target region of the *Sun1b* gene was amplified via genomic PCR using the following primers (Forward: 5'-GGCTGCGTCAGACTCCATTA-3'; Reverse: 5'-TTGAGTTAAACCCAGCGCCT-3'). The amplicon was then sequenced by Sanger sequencing (GENEWIZ) using the forward primer. Morphant fish were obtained by injecting 2.5-5ng of NT (5'-CCTCTTACCTCAGTTACAATTTATA-3', GeneTools, LLC) or SUN1 (5'-CGCAGTTTGACCATCAGTTTCTACA-3', GeneTools, LLC) morpholinos into *Tg(fli:LifeAct-GFP)* embryos at the 1-cell stage. Fish were grown in E3 medium at 28.5°C to either 24 or 33-34 hpf.

bioRxiv preprint doi: https://doi.org/10.1101/2021.08.11.455980; this version posted August 11, 2021. The copyright holder for this preprint (which was not certified by peer review) is the author/funder, who has granted bioRxiv a license to display the preprint in perpetuity. It is made available under aCC-BY-NC-ND 4.0 International license.

Zebrafish imaging

Dechorionated embryos were incubated in ice cold 4% PFA at 4°C overnight or RT for 2h. Embryos were rinsed in PBS and a fine probe was used to de-yolk and a small blade to separate the trunk from the cephalic region. Samples were mounted using Prolong Diamond Antifade mounting medium (P36961, Life Technology) and the coverslip was sealed with petroleum jelly. Imaging was at RT using a UPlanSApo 20x oil-immersion objective (NA 0.58) or a UPlanSApo 60x oil-immersion objective (NA 1.40) with an additional 3x magnification, for a total magnification of 180x. Ectopic sprouts were measured by counting sprouts from the dorsal aorta at non-consistent intervals sprouts emanating from individual ISVs. Filopodia length was measured by drawing a line from the filopodia base to the tip. Filopodia number was measured by counting the number of filopodia and normalizing to the total vessel length.

For live imaging of zebrafish, fish were dechorionated and then anesthetized with 1x Tricaine in E3 for 5 min. Fish were embedded in 0.5% agarose in 1x Tricaine-E3 medium on a glass-bottomed plate in a stage-top incubator (TOKAI HIT, WSKM) at 28.5°C. Images were acquired using a UPlanSApo 40x air objective (NA 0.95) every 15min for 10-15h. ISVs that did not reach the DLAV or connected at non-consistent intervals were considered to have a missing or aberrant DLAV connection if at least 1 ISV posterior to the scored ISV made a normal connection.

Statistics

Student's two-tailed *t* test was used to determine statistical significance in experiments with 2 groups. One-way ANOVA with Tukey's multiple comparisons test was used to determine statistical significance for experiments with 3 or more groups,

bioRxiv preprint doi: https://doi.org/10.1101/2021.08.11.455980; this version posted August 11, 2021. The copyright holder for this preprint (which was not certified by peer review) is the author/funder, who has granted bioRxiv a license to display the preprint in perpetuity. It is made available under aCC-BY-NC-ND 4.0 International license.

and X^2 was used for categorical data. Error bars represent the mean ± standard deviation. Statistical tests and graphs were made using the Prism 9 software (GraphPad Software).

ACKNOWLEGMENTS

We thank the UNC Hooker Imaging Core, Michelle Altemara and staff at the Zebrafish Aquaculture Core, Kaitlyn Quigley for fish room support, Aaron Friedman for mouse room support, and Steve Rogers, Yosuke Mukouyama, Nick Buglak, and Bautch Lab members for critical discussion and feedback.

AUTHOR CONTRIBUTIONS

Danielle B Buglak (DBB) and Victoria L Bautch (VLB) conceptualized the work; DBB, Ariel L Gold (ALG), Allison P Marvin (APM), Shea N Ricketts (SNR), Morgan Oatley (MO), Natalie T Tanke (NTT), and Bryan N Johnson (BNJ) performed and analyzed experiments; DBB and VLB wrote and edited the manuscript; VLB provided study supervision and oversight.

FUNDING

This work was supported by grants from the National Institutes of Health (R35 HL139950 to VLB), the Integrated Vascular Biology Training Grant (5T32HL069768-17, DBB), an American Heart Association Predoctoral Fellowship (19PRE34380887 to DBB), an NIH F31 Predoctoral Fellowship (1F31HL156527-01 to NTT), and an American Heart Association Postdoctoral Fellowship (AHA829371 to MO).

DECLARATION OF INTERESTS: None.

bioRxiv preprint doi: https://doi.org/10.1101/2021.08.11.455980; this version posted August 11, 2021. The copyright holder for this preprint (which was not certified by peer review) is the author/funder, who has granted bioRxiv a license to display the preprint in perpetuity. It is made available under aCC-BY-NC-ND 4.0 International license.

REFERENCES

Abu Taha, A., & Schnittler, H.-J. 2014. Dynamics between actin and the VE-cadherin/catenin complex: novel aspects of the ARP2/3 complex in regulation of endothelial junctions. *Cell Adh. Migr.* 8(2): p.125–35. http://www.ncbi.nlm.nih.gov/pubmed/24621569.

Angulo-Urarte, A. et al. 2018. Endothelial cell rearrangements during vascular patterning require PI3-kinase-mediated inhibition of actomyosin contractility. *Nat. Commun.* 9(1): p.4826. http://www.ncbi.nlm.nih.gov/pubmed/30446640.

Arganda-Carreras, I., Fernández-González, R., Muñoz-Barrutia, A., & Ortiz-De-Solorzano, C. 2010. 3D reconstruction of histological sections: Application to mammary gland tissue. *Microsc. Res. Tech.* 73(11): p.1019–1029. https://onlinelibrary.wiley.com/doi/10.1002/jemt.20829.

Bautch, V.L., & Caron, K.M. 2015. Blood and lymphatic vessel formation. *Cold Spring Harb. Perspect. Biol.* 7(3): p.a008268.

Birukova, A.A., Adyshev, D., Gorshkov, B., Bokoch, G.M., Birukov, K.G., & Verin, A.D. 2006. GEF-H1 is involved in agonist-induced human pulmonary endothelial barrier dysfunction. *Am. J. Physiol. Lung Cell. Mol. Physiol.* 290(3): p.L540-8. http://www.ncbi.nlm.nih.gov/pubmed/16257999.

Birukova, A.A., Liu, F., Garcia, J.G.N., & Verin, A.D. 2004. Protein kinase A attenuates endothelial cell barrier dysfunction induced by microtubule disassembly. *Am. J. Physiol. Lung Cell. Mol. Physiol.* 287(1): p.L86-93. http://www.ncbi.nlm.nih.gov/pubmed/15003930.

Blum, Y., Belting, H.-G., Ellertsdottir, E., Herwig, L., Lüders, F., & Affolter, M. 2008. Complex cell rearrangements during intersegmental vessel sprouting and vessel fusion in the zebrafish embryo. *Dev. Biol.* 316(2): p.312–22. http://www.ncbi.nlm.nih.gov/pubmed/18342303.

Buglak, D.B., Kushner, E.J., Marvin, A.P., Davis, K.L., & Bautch, V.L. 2020. Excess centrosomes disrupt vascular lumenization and endothelial cell adherens junctions. *Angiogenesis* 23(4): p.567–575. http://www.ncbi.nlm.nih.gov/pubmed/32699963.

Capell, B.C., & Collins, F.S. 2006. Human laminopathies: nuclei gone genetically awry. *Nat. Rev. Genet.* 7(12): p.940–52. http://www.ncbi.nlm.nih.gov/pubmed/17139325.

Carmeliet, P., & Jain, R.K. 2011. Molecular mechanisms and clinical applications of angiogenesis. *Nature* 473(7347): p.298–307.

Chancellor, T.J., Lee, J., Thodeti, C.K., & Lele, T. 2010. Actomyosin tension exerted on the nucleus through nesprin-1 connections influences endothelial cell adhesion, migration, and cyclic strain-induced reorientation. *Biophys. J.* 99(1): p.115–23. http://www.ncbi.nlm.nih.gov/pubmed/20655839.

bioRxiv preprint doi: https://doi.org/10.1101/2021.08.11.455980; this version posted August 11, 2021. The copyright holder for this preprint (which was not certified by peer review) is the author/funder, who has granted bioRxiv a license to display the preprint in perpetuity. It is made available under aCC-BY-NC-ND 4.0 International license.

Chang, W., Antoku, S., Östlund, C., Worman, H.J., & Gundersen, G.G. 2015. Linker of nucleoskeleton and cytoskeleton (LINC) complex-mediated actin-dependent nuclear positioning orients centrosomes in migrating myoblasts. *Nucleus* 6(1): p.77–88. http://www.ncbi.nlm.nih.gov/pubmed/25587885.

Chang, W., Wang, Y., Luxton, G.W.G., Östlund, C., Worman, H.J., & Gundersen, G.G. 2019. Imbalanced nucleocytoskeletal connections create common polarity defects in progeria and physiological aging. *Proc. Natl. Acad. Sci. U. S. A.* 116(9): p.3578–3583. http://www.ncbi.nlm.nih.gov/pubmed/30808750.

Chen, C.-Y., Chi, Y.-H., Mutalif, R.A., Starost, M.F., Myers, T.G., Anderson, S.A., Stewart, C.L., & Jeang, K.-T. 2012. Accumulation of the Inner Nuclear Envelope Protein Sun1 Is Pathogenic in Progeric and Dystrophic Laminopathies. *Cell* 149(3): p.565–577. https://linkinghub.elsevier.com/retrieve/pii/S0092867412004011.

Chen, Z.-J., Wang, W.-P., Chen, Y.-C., Wang, J.-Y., Lin, W.-H., Tai, L.-A., Liou, G.-G., Yang, C.-S., & Chi, Y.-H. 2014. Dysregulated interactions between lamin A and SUN1 induce abnormalities in the nuclear envelope and endoplasmic reticulum in progeric laminopathies. *J. Cell Sci.* 127(Pt 8): p.1792–804. http://www.ncbi.nlm.nih.gov/pubmed/24522183.

Chong, D.C., Yu, Z., Brighton, H.E., Bear, J.E., & Bautch, V.L. 2017. Tortuous Microvessels Contribute to Wound Healing via Sprouting Angiogenesis. *Arterioscler. Thromb. Vasc. Biol.* 37(10): p.1903–1912. http://www.ncbi.nlm.nih.gov/pubmed/28838921.

Dejana, E. 2004. Endothelial cell-cell junctions: happy together. *Nat. Rev. Mol. Cell Biol.* 5(4): p.261–70. http://www.ncbi.nlm.nih.gov/pubmed/15071551.

Dejana, E., & Vestweber, D. 2013. The role of VE-cadherin in vascular morphogenesis and permeability control. *Prog. Mol. Biol. Transl. Sci.* 116: p.119–44. http://www.ncbi.nlm.nih.gov/pubmed/23481193.

Denis, K.B., Cabe, J.I., Danielsson, B.E., Tieu, K. V, Mayer, C.R., & Conway, D.E. 2021. The LINC complex is required for endothelial cell adhesion and adaptation to shear stress and cyclic stretch. *Mol. Biol. Cell*: p.mbcE20110698. http://www.ncbi.nlm.nih.gov/pubmed/34191529.

Dubrovskyi, O., Birukova, A.A., & Birukov, K.G. 2013. Measurement of local permeability at subcellular level in cell models of agonist- and ventilator-induced lung injury. *Lab. Invest.* 93(2): p.254–63. http://www.ncbi.nlm.nih.gov/pubmed/23212101.

Eriksson, M., Brown, W.T., Gordon, L.B., Glynn, M.W., Singer, J., Scott, L., Erdos, M.R., Robbins, C.M., Moses, T.Y., Berglund, P., Dutra, A., Pak, E., Durkin, S., Csoka, A.B., Boehnke, M., Glover, T.W., & Collins, F.S. 2003. Recurrent de novo point mutations in lamin A cause Hutchinson-Gilford progeria syndrome. *Nature* 423(6937): p.293–8. http://www.ncbi.nlm.nih.gov/pubmed/12714972.

Esser, S., Lampugnani, M.G., Corada, M., Dejana, E., & Risau, W. 1998. Vascular endothelial growth factor induces VE-cadherin tyrosine phosphorylation in endothelial

bioRxiv preprint doi: https://doi.org/10.1101/2021.08.11.455980; this version posted August 11, 2021. The copyright holder for this preprint (which was not certified by peer review) is the author/funder, who has granted bioRxiv a license to display the preprint in perpetuity. It is made available under aCC-BY-NC-ND 4.0 International license.

cells. *J. Cell Sci.* 111 (Pt 1: p.1853–65. http://www.ncbi.nlm.nih.gov/pubmed/9625748.

Graham, D.M., Andersen, T., Sharek, L., Uzer, G., Rotherberg, K., Hoffman, B.D., Rubin, J., Balland, M., Bear, J.E., & Burridge, K. 2018. Enucleated cells reveal differential roles of the nucleus in cell migration, polarity, and mechanotransduction. *J. Cell Biol.*: p.jcb.201706097.

Guilluy, C., Osborne, L.D., Van Landeghem, L., Sharek, L., Superfine, R., Garcia-Mata, R., & Burridge, K. 2014. Isolated nuclei adapt to force and reveal a mechanotransduction pathway in the nucleus. *Nat. Cell Biol.* 16(4): p.376–81. http://www.ncbi.nlm.nih.gov/pubmed/24609268.

Haque, F., Lloyd, D.J., Smallwood, D.T., Dent, C.L., Shanahan, C.M., Fry, A.M., Trembath, R.C., & Shackleton, S. 2006. SUN1 interacts with nuclear lamin A and cytoplasmic nesprins to provide a physical connection between the nuclear lamina and the cytoskeleton. *Mol. Cell. Biol.* 26(10): p.3738–51. http://www.ncbi.nlm.nih.gov/pubmed/16648470.

Haque, F., Mazzeo, D., Patel, J.T., Smallwood, D.T., Ellis, J.A., Shanahan, C.M., & Shackleton, S. 2010. Mammalian SUN protein interaction networks at the inner nuclear membrane and their role in laminopathy disease processes. *J. Biol. Chem.* 285(5): p.3487–98. http://www.ncbi.nlm.nih.gov/pubmed/19933576.

Hübner, K., Cabochette, P., Diéguez-Hurtado, R., Wiesner, C., Wakayama, Y., Grassme, K.S., Hubert, M., Guenther, S., Belting, H.-G., Affolter, M., Adams, R.H., Vanhollebeke, B., & Herzog, W. 2018. Wnt/β-catenin signaling regulates VE-cadherin-mediated anastomosis of brain capillaries by counteracting S1pr1 signaling. *Nat. Commun.* 9(1): p.4860. http://www.ncbi.nlm.nih.gov/pubmed/30451830.

Huveneers, S., Oldenburg, J., Spanjaard, E., van der Krogt, G., Grigoriev, I., Akhmanova, A., Rehmann, H., & de Rooij, J. 2012. Vinculin associates with endothelial VE-cadherin junctions to control force-dependent remodeling. *J. Cell Biol.* 196(5): p.641–52. http://www.ncbi.nlm.nih.gov/pubmed/22391038.

Jaqaman, K., Loerke, D., Mettlen, M., Kuwata, H., Grinstein, S., Schmid, S.L., & Danuser, G. 2008. Robust single-particle tracking in live-cell time-lapse sequences. *Nat. Methods* 5(8): p.695–702. http://www.ncbi.nlm.nih.gov/pubmed/18641657.

Ketema, M., Wilhelmsen, K., Kuikman, I., Janssen, H., Hodzic, D., & Sonnenberg, A. 2007. Requirements for the localization of nesprin-3 at the nuclear envelope and its interaction with plectin. *J. Cell Sci.* 120(Pt 19): p.3384–94. http://www.ncbi.nlm.nih.gov/pubmed/17881500.

King, S.J., Nowak, K., Suryavanshi, N., Holt, I., Shanahan, C.M., & Ridley, A.J. 2014. Nesprin-1 and nesprin-2 regulate endothelial cell shape and migration. *Cytoskeleton (Hoboken).* 71(7): p.423–34. http://www.ncbi.nlm.nih.gov/pubmed/24931616.

Komarova, Y.A., Huang, F., Geyer, M., Daneshjou, N., Garcia, A., Idalino, L., Kreutz, B., Mehta, D., & Malik, A.B. 2012. VE-cadherin signaling induces EB3 phosphorylation to suppress microtubule growth and assemble adherens junctions. *Mol. Cell* 48(6): p.914–

bioRxiv preprint doi: https://doi.org/10.1101/2021.08.11.455980; this version posted August 11, 2021. The copyright holder for this preprint (which was not certified by peer review) is the author/funder, who has granted bioRxiv a license to display the preprint in perpetuity. It is made available under aCC-BY-NC-ND 4.0 International license.

925.

Kushner, E.J., & Bautch, V.L. 2013. Building blood vessels in development and disease. *Curr. Opin. Hematol.* 20(3): p.231–6. http://www.ncbi.nlm.nih.gov/pubmed/23567339.

Kushner, E.J., Ferro, L.S., Liu, J.-Y., Durrant, J.R., Rogers, S.L., Dudley, A.C., & Bautch, V.L. 2014. Excess centrosomes disrupt endothelial migration via centrosome scattering. *J. Cell Biol.* 206(2): p.257–272.

Kushner, E.J., Ferro, L.S., Yu, Z., & Bautch, V.L. 2016. Excess centrosomes perturb dynamic endothelial cell repolarization during blood vessel formation. *Mol. Biol. Cell* 27(12): p.1911–1920.

Lei, K., Zhang, X., Ding, X., Guo, X., Chen, M., Zhu, B., Xu, T., Zhuang, Y., Xu, R., & Han, M. 2009. SUN1 and SUN2 play critical but partially redundant roles in anchoring nuclei in skeletal muscle cells in mice. *PNAS* 106(25): p.10207–10212.

Linkert, M., Rueden, C.T., Allan, C., Burel, J.-M., Moore, W., Patterson, A., Loranger, B., Moore, J., Neves, C., MacDonald, D., Tarkowska, A., Sticco, C., Hill, E., Rossner, M., Eliceiri, K.W., & Swedlow, J.R. 2010. Metadata matters: access to image data in the real world. *J. Cell Biol.* 189(5): p.777–782. https://rupress.org/jcb/article/189/5/777/35828/Metadata-matters-access-to-image-data-in-the-real.

McGee, M.D., Rillo, R., Anderson, A.S., & Starr, D.A. 2006. UNC-83 IS a KASH protein required for nuclear migration and is recruited to the outer nuclear membrane by a physical interaction with the SUN protein UNC-84. *Mol. Biol. Cell* 17(4): p.1790–801. http://www.ncbi.nlm.nih.gov/pubmed/16481402.

Morgan, J.T., Pfeiffer, E.R., Thirkill, T.L., Kumar, P., Peng, G., Fridolfsson, H.N., Douglas, G.C., Starr, D.A., & Barakat, A.I. 2011. Nesprin-3 regulates endothelial cell morphology, perinuclear cytoskeletal architecture, and flow-induced polarization. *Mol. Biol. Cell* 22(22): p.4324–34. http://www.ncbi.nlm.nih.gov/pubmed/21937718.

Nakatsu, M.N., & Hughes, C.C.W. 2008. An optimized three-dimensional in vitro model for the analysis of angiogenesis. *Methods Enzymol.* 443: p.65–82.

Nesmith, J.E., Chappell, J.C., Cluceru, J.G., & Bautch, V.L. 2017. Blood vessel anastomosis is spatially regulated by Flt1 during angiogenesis. *Development* 144(5): p.889–896. http://www.ncbi.nlm.nih.gov/pubmed/28246215.

Neto, F., Klaus-Bergmann, A., Ong, Y.T., Alt, S., Vion, A.-C., Szymborska, A., Carvalho, J.R., Hollfinger, I., Bartels-Klein, E., Franco, C.A., Potente, M., & Gerhardt, H. 2018. YAP and TAZ regulate adherens junction dynamics and endothelial cell distribution during vascular development. *Elife* 7. http://www.ncbi.nlm.nih.gov/pubmed/29400648.

Olive, M., Harten, I., Mitchell, R., Beers, J.K., Djabali, K., Cao, K., Erdos, M.R., Blair, C., Funke, B., Smoot, L., Gerhard-Herman, M., Machan, J.T., Kutys, R., Virmani, R., Collins, F.S., Wight, T.N., Nabel, E.G., & Gordon, L.B. 2010. Cardiovascular pathology in Hutchinson-Gilford progeria: correlation with the vascular pathology of aging.

bioRxiv preprint doi: https://doi.org/10.1101/2021.08.11.455980; this version posted August 11, 2021. The copyright holder for this preprint (which was not certified by peer review) is the author/funder, who has granted bioRxiv a license to display the preprint in perpetuity. It is made available under aCC-BY-NC-ND 4.0 International license.

Arterioscler. Thromb. Vasc. Biol. 30(11): p.2301–9. http://www.ncbi.nlm.nih.gov/pubmed/20798379.

Osmanagic-Myers, S., Kiss, A., Manakanatas, C., Hamza, O., Sedlmayer, F., Szabo, P.L., Fischer, I., Fichtinger, P., Podesser, B.K., Eriksson, M., & Foisner, R. 2019. Endothelial progerin expression causes cardiovascular pathology through an impaired mechanoresponse. *J. Clin. Invest.* 129(2): p.531–545. http://www.ncbi.nlm.nih.gov/pubmed/30422822.

Ostlund, C., Folker, E.S., Choi, J.C., Gomes, E.R., Gundersen, G.G., & Worman, H.J. 2009. Dynamics and molecular interactions of linker of nucleoskeleton and cytoskeleton (LINC) complex proteins. *J. Cell Sci.* 122(Pt 22): p.4099–108. http://www.ncbi.nlm.nih.gov/pubmed/19843581.

Padmakumar, V.C., Libotte, T., Lu, W., Zaim, H., Abraham, S., Noegel, A.A., Gotzmann, J., Foisner, R., & Karakesisoglou, I. 2005. The inner nuclear membrane protein Sun1 mediates the anchorage of Nesprin-2 to the nuclear envelope. *J. Cell Sci.* 118(Pt 15): p.3419–30. http://www.ncbi.nlm.nih.gov/pubmed/16079285.

Rauzi, M., Lenne, P.-F., & Lecuit, T. 2010. Planar polarized actomyosin contractile flows control epithelial junction remodelling. *Nature* 468(7327): p.1110–4.

Rho, S.-S., Ando, K., & Fukuhara, S. 2017. Dynamic Regulation of Vascular Permeability by Vascular Endothelial Cadherin-Mediated Endothelial Cell-Cell Junctions. *J. Nippon Med. Sch.* 84(4): p.148–159. http://www.ncbi.nlm.nih.gov/pubmed/28978894.

De Sandre-Giovannoli, A. 2003. Lamin A Truncation in Hutchinson-Gilford Progeria. *Science (80-.).* 300(5628): p.2055–2055. https://www.sciencemag.org/lookup/doi/10.1126/science.1084125.

Sauteur, L., Affolter, M., & Belting, H.-G. 2017. Distinct and redundant functions of Esam and VE-cadherin during vascular morphogenesis. *Development*. https://journals.biologists.com/dev/article/doi/10.1242/dev.140038/264230/Distinct-and-redundant-functions-of-Esam-and-VE.

Sauteur, L., Krudewig, A., Herwig, L., Ehrenfeuchter, N., Lenard, A., Affolter, M., & Belting, H.-G. 2014. Cdh5/VE-cadherin Promotes Endothelial Cell Interface Elongation via Cortical Actin Polymerization during Angiogenic Sprouting. *Cell Rep.* 9(2): p.504–513. https://linkinghub.elsevier.com/retrieve/pii/S2211124714008031.

Schindelin, J., Arganda-Carreras, I., Frise, E., Kaynig, V., Longair, M., Pietzsch, T., Preibisch, S., Rueden, C., Saalfeld, S., Schmid, B., Tinevez, J.-Y., White, D.J., Hartenstein, V., Eliceiri, K., Tomancak, P., & Cardona, A. 2012. Fiji: an open-source platform for biological-image analysis. *Nat. Methods* 9(7): p.676–682. http://www.nature.com/articles/nmeth.2019.

Schneider, M., Lu, W., Neumann, S., Brachner, A., Gotzmann, J., Noegel, A.A., & Karakesisoglou, I. 2011. Molecular mechanisms of centrosome and cytoskeleton anchorage at the nuclear envelope. *Cell. Mol. Life Sci.* 68(9): p.1593–610.

bioRxiv preprint doi: https://doi.org/10.1101/2021.08.11.455980; this version posted August 11, 2021. The copyright holder for this preprint (which was not certified by peer review) is the author/funder, who has granted bioRxiv a license to display the preprint in perpetuity. It is made available under aCC-BY-NC-ND 4.0 International license.

http://www.ncbi.nlm.nih.gov/pubmed/20922455.

Sehrawat, S., Cullere, X., Patel, S., Italiano, J., & Mayadas, T.N. 2008. Role of Epac1, an exchange factor for Rap GTPases, in endothelial microtubule dynamics and barrier function. *Mol. Biol. Cell* 19(3): p.1261–70. http://www.ncbi.nlm.nih.gov/pubmed/18172027.

Sehrawat, S., Ernandez, T., Cullere, X., Takahashi, M., Ono, Y., Komarova, Y., & Mayadas, T.N. 2011. AKAP9 regulation of microtubule dynamics promotes Epac1-induced endothelial barrier properties. *Blood* 117(2): p.708–18. http://www.ncbi.nlm.nih.gov/pubmed/20952690.

Sörensen, I., Adams, R.H., & Gossler, A. 2009. DLL1-mediated Notch activation regulates endothelial identity in mouse fetal arteries. *Blood* 113(22): p.5680–5688. https://ashpublications.org/blood/article/113/22/5680/107805/DLL1mediated-Notch-activation-regulates.

Starr, D.A., & Fridolfsson, H.N. 2010. Interactions between nuclei and the cytoskeleton are mediated by SUN-KASH nuclear-envelope bridges. *Annu. Rev. Cell Dev. Biol.* 26: p.421–44. http://www.ncbi.nlm.nih.gov/pubmed/20507227.

Stehbens, S.J., Akhmanova, A., & Yap, A.S. 2009. Microtubules and cadherins: a neglected partnership. *Front. Biosci. (Landmark Ed.* 14: p.3159–67. http://www.ncbi.nlm.nih.gov/pubmed/19273264.

Stehbens, S.J., Paterson, A.D., Crampton, M.S., Shewan, A.M., Ferguson, C., Akhmanova, A., Parton, R.G., & Yap, A.S. 2006. Dynamic microtubules regulate the local concentration of E-cadherin at cell-cell contacts. *J. Cell Sci.* 119(Pt 9): p.1801–11. http://www.ncbi.nlm.nih.gov/pubmed/16608875.

Stewart-Hutchinson, P.J., Hale, C.M., Wirtz, D., & Hodzic, D. 2008. Structural requirements for the assembly of LINC complexes and their function in cellular mechanical stiffness. *Exp. Cell Res.* 314(8): p.1892–905. http://www.ncbi.nlm.nih.gov/pubmed/18396275.

Stewart, R.M., Zubek, A.E., Rosowski, K.A., Schreiner, S.M., Horsley, V., & King, M.C. 2015. Nuclear-cytoskeletal linkages facilitate cross talk between the nucleus and intercellular adhesions. *J. Cell Biol.* 209(3): p.403–18. http://www.ncbi.nlm.nih.gov/pubmed/25963820.

Thakar, K., May, C.K., Rogers, A., & Carroll, C.W. 2017. Opposing roles for distinct LINC complexes in regulation of the small GTPase RhoA. *Mol. Biol. Cell* 28(1): p.182–191. http://www.ncbi.nlm.nih.gov/pubmed/28035049.

Tkachenko, E., Gutierrez, E., Saikin, S.K., Fogelstrand, P., Kim, C., Groisman, A., & Ginsberg, M.H. 2013. The nucleus of endothelial cell as a sensor of blood flow direction. *Biol. Open* 2(10): p.1007–12. http://www.ncbi.nlm.nih.gov/pubmed/24167710.

Vasileva, E., & Citi, S. 2018. The role of microtubules in the regulation of epithelial junctions. *Tissue barriers* 6(3): p.1539596.

bioRxiv preprint doi: https://doi.org/10.1101/2021.08.11.455980; this version posted August 11, 2021. The copyright holder for this preprint (which was not certified by peer review) is the author/funder, who has granted bioRxiv a license to display the preprint in perpetuity. It is made available under aCC-BY-NC-ND 4.0 International license.

http://www.ncbi.nlm.nih.gov/pubmed/30395792.

Verin, A.D., Birukova, A., Wang, P., Liu, F., Becker, P., Birukov, K., & Garcia, J.G. 2001. Microtubule disassembly increases endothelial cell barrier dysfunction: role of MLC phosphorylation. *Am. J. Physiol. Lung Cell. Mol. Physiol.* 281(3): p.L565-74. http://www.ncbi.nlm.nih.gov/pubmed/11504682.

Waterman-Storer, C.M., Worthylake, R.A., Liu, B.P., Burridge, K., & Salmon, E.D. 1999. Microtubule growth activates Rac1 to promote lamellipodial protrusion in fibroblasts. *Nat. Cell Biol.* 1(1): p.45–50. http://www.ncbi.nlm.nih.gov/pubmed/10559863.

Wittmann, T., Bokoch, G.M., & Waterman-Storer, C.M. 2003. Regulation of leading edge microtubule and actin dynamics downstream of Rac1. *J. Cell Biol.* 161(5): p.845–51. http://www.ncbi.nlm.nih.gov/pubmed/12796474.

Wright, C.E., Kushner, E.J., Du, Q., & Bautch, V.L. 2015. LGN directs interphase endothelial cell behavior via the microtubule network. *PLoS One* 10(9): p.1–15.

Wylie, L.A., Mouillesseaux, K.P., Chong, D.C., & Bautch, V.L. 2018. Developmental SMAD6 loss leads to blood vessel hemorrhage and disrupted endothelial cell junctions. *Dev. Biol.* 442(2): p.199–209. http://www.ncbi.nlm.nih.gov/pubmed/30098998.

Zhang, X., Lei, K., Yuan, X., Wu, X., Zhuang, Y., Xu, T., Xu, R., & Han, M. 2009. SUN1/2 and Syne/Nesprin-1/2 complexes connect centrosome to the nucleus during neurogenesis and neuronal migration in mice. *Neuron* 64(2): p.173–87. http://www.ncbi.nlm.nih.gov/pubmed/19874786.

Zhu, R., Antoku, S., & Gundersen, G.G. 2017. Centrifugal Displacement of Nuclei Reveals Multiple LINC Complex Mechanisms for Homeostatic Nuclear Positioning. *Curr. Biol.* 27(20): p.3097-3110.e5. http://www.ncbi.nlm.nih.gov/pubmed/28988861.

bioRxiv preprint doi: https://doi.org/10.1101/2021.08.11.455980; this version posted August 11, 2021. The copyright holder for this preprint (which was not certified by peer review) is the author/funder, who has granted bioRxiv a license to display the preprint in perpetuity. It is made available under aCC-BY-NC-ND 4.0 International license.

FIGURE LEGENDS

Figure 1. The nuclear LINC protein SUN1 regulates vascular development.

(a) Schematic of tamoxifen-induced excision of exon 4 of *Sun1* in pups from cross of *Sun1*$^{fl/fl}$ X *Sun1*$^{fl/+}$*;Cdh5CreERT2* mice. **(b)** Representative images P7 mouse retinas of indicated genotypes, stained for IB4 (isolectin). Scale bar, 500µm. **(c)** Higher magnification representative images at the vascular front of P7 mouse retinas of indicated genotypes, stained for IB4 (isolectin). Scale bar, 150µm. **(d)** Quantification of vessel network radial expansion in **b**. Controls, N=17 mice (27 retinas) from 3 independent litters. *Sun1*^{iECKO}, N=6 mice (12 retinas) from 3 independent litters. **(e)** Quantification of vascular density in **c**. Controls, N=12 mice (18 retinas) from 2 independent litters. *Sun1*$^{iECKO/}$, N=4 mice (8 retinas) from 3 independent litters. **(f)** Representative images of IB4 (isolectin) (green, vessels) and VE-cadherin (white, junctions) staining in P7 retinas of indicated genotypes. Scale bar, 50µm. Statistics: student's two-tailed *t* test. *, *p*≤0.05; ****, *p*≤0.0001.

Figure 2. SUN1 stabilizes endothelial cell-cell junctions and regulates barrier function.

(a) Representative images of HUVEC with indicated knockdowns in monolayers. Endothelial cells were stained for DAPI (cyan, DNA) and VE-cadherin (white, junctions). Insets show junctions. Scale bar, 10µm. **(b)** Representative graph of impedance measured by RTCA. **(c)** Quantification of % change in cell index for RTCA measured at 5h. Normalized to NT cell index. N=5 replicates. **(d)** Representative images of HUVEC with indicated siRNAs showing adherens following EDTA washout. Endothelial cells were stained for DRAQ7 (cyan, DNA) and VE-cadherin (white, junctions). Insets show junctions. Scale bar, 20µm. **(e)** Quantification of VE-cadherin line scans at 20 min, 40

bioRxiv preprint doi: https://doi.org/10.1101/2021.08.11.455980; this version posted August 11, 2021. The copyright holder for this preprint (which was not certified by peer review) is the author/funder, who has granted bioRxiv a license to display the preprint in perpetuity. It is made available under aCC-BY-NC-ND 4.0 International license.

min, and 60 min post EDTA washout in **d**. Representative replicate. N=3 replicates. **(f)** Representative images of HUVEC with indicated siRNAs showing VE-cadherin staining after internalization assay. Endothelial cells were stained for DRAQ7 (cyan, DNA), VE-cadherin (white, junctions), and Phalloidin (green, actin). Scale bar, 20μm. **(g)** Quantification of area of internalized VE-cadherin in **f**. Data compiled from N=3 replicates. Statistics: student's two-tailed *t* test. ns, not significant; *, $p \leq 0.05$, **; $p \leq 0.01$, ****; $p \leq 0.0001$.

Figure 3. SUN1 regulates endothelial cell contractility.

(a) Representative images of HUVEC with indicated siRNAs and indicated treatments. Endothelial cells were stained for DAPI (cyan, DNA) and VE-cadherin (white, junctions). Insets show junctions. Scale bar, 20μm. **(b)** Quantification of VE-cadherin line scans for treatments shown in **a**. Data compiled from N=3 replicates. **(c)** Representative images of HUVEC with indicated siRNAs and indicated treatments. Endothelial cells were stained for DAPI (cyan, DNA) and VE-cadherin (white, junctions). Insets show junctions. Scale bar, 20μm. **(d)** Quantification of VE-cadherin line scans for treatments shown in **c**. Data compiled from N=3 replicates. **(e)** Representative images of HUVEC with indicated siRNAs and indicated treatments. Endothelial cells were stained for DAPI (cyan, DNA) and VE-cadherin (white, junctions). Insets show junctions. Scale bar, 20μm. **(f)** Quantification of VE-cadherin line scans for treatments shown in **e**. Data compiled from N=3 replicates replicates. Statistics: one-way ANOVA with Tukey's correction. ns, not significant; ****, $p \leq 0.0001$.

bioRxiv preprint doi: https://doi.org/10.1101/2021.08.11.455980; this version posted August 11, 2021. The copyright holder for this preprint (which was not certified by peer review) is the author/funder, who has granted bioRxiv a license to display the preprint in perpetuity. It is made available under aCC-BY-NC-ND 4.0 International license.

Figure 4. SUN1 regulates microtubule localization and dynamics in endothelial cells.

(a) Representative images of HUVEC with indicated siRNAs and indicated treatments. Endothelial cells were stained for DAPI (cyan, DNA) and VE-cadherin (white, junctions). Insets show junctions. Scale bar, 20μm. **(b)** Quantification of VE-cadherin line scans for treatments shown in **a**. Data compiled from N=3 replicates. **(c)** Representative images of HUVEC with indicated siRNAs and antibody staining. Endothelial cells were stained for α-tubulin (green, microtubules), DAPI (cyan, DNA), and VE-cadherin (white, junctions). Yellow insets show α-tubulin at the nucleus, red insets show α-tubulin at the periphery. Scale bar, 20μm. Scale bar for insets, 5μm. **(d)** Quantification of nuclear α-tubulin area normalized to MTOC α-tubulin area shown in **c**. Data compiled from N=3 replicates. **(e)** Quantification of peripheral α-tubulin area normalized to MTOC α-tubulin area shown in **c**. Data compiled from N=3 replicates. Statistics: one-way ANOVA with Tukey's correction. ns, not significant; ****, $p \leq 0.0001$.

Figure 5. Nuclear SUN1 is required for sprouting angiogenesis.

(a) Representative images HUVEC with indicated siRNAs in 3D angiogenic sprouting assay. Sprouts were stained for Phalloidin (actin) and then depth encoded such that cooler colors are further in the Z-plane and warmer colors are closer in the Z-plane. Scale bar, 100μm. **(b)** Quantification of average sprout length of 3D angiogenic sprouts shown in **a**. Data compiled from N=5 replicates. **(c)** Quantification of branches/mm of 3D angiogenic sprouts shown in **a**. Data compiled from N=5 replicates. Statistics: student's two-tailed *t* test. ****, $p \leq 0.0001$. **(d)** Stills from Movie S1 and Movie S2 showing sprouting dynamics of HUVEC with indicated siRNAs over 50h. Scale bar, 50μm. **(e)** Quantification of HUVEC sprout extensions and retractions shown in **d**. Data compiled

bioRxiv preprint doi: https://doi.org/10.1101/2021.08.11.455980; this version posted August 11, 2021. The copyright holder for this preprint (which was not certified by peer review) is the author/funder, who has granted bioRxiv a license to display the preprint in perpetuity. It is made available under aCC-BY-NC-ND 4.0 International license.

from N=3 replicates (NT, n=101 sprouts; SUN1 KD, n=77 sprouts). Statistics: χ^2 analysis.

Figure 6. SUN1 regulates actin dynamics and angiogenic sprout extension *in vivo*.

(a) Representative images of zebrafish embryos at 24 hpf with indicated genotypes and morpholino treatments; anterior to left. *Tg(fli:LifeAct-GFP)* (green, vessels). Insets show single intersegmental vessel (ISV). Arrows point to ectopic sprouts. Scale bar, 50µm. **(b)** Quantification of percentage of fish with ectopic sprouts shown in **a**. Data compiled from 3 independent experiments for morphant fish (NT, n=24 fish; SUN1b MO, n=23 fish) and 3 independent experiments for mutant fish (*Sun1b*$^{+/+}$, n=10 fish; *Sun1b*$^{sa33109/sa33109}$, n=10 fish). Statistics: χ^2 analysis. **(c)** Representative images of zebrafish embryos at 34 hpf with indicated morpholino treatments; anterior to left. *Tg(fli:LifeAct-GFP)* (green, vessels). Insets show ISVs with filopodia. Arrows point to filopodia. Scale bar, 20µm. **(d)** Quantification of filopodia number shown in **c**. Data compiled from N=3 replicates (NT, 15 fish; SUN1b MO, n=20 fish; 3 areas measured/fish). **(e)** Quantification of average filopodia length shown in **c**. Data compiled from N=3 replicates (NT, 15 fish; SUN1b MO, n=20 fish; 3 areas measured/fish). **(f)** Representative images of zebrafish embryos at 34 hpf with indicated genotypes; anterior to left. *Tg(fli:LifeAct-GFP)* (green, vessels). Insets show ISVs with filopodia. Arrows point to filopodia. Scale bar, 20µm. **(g)** Quantification of filopodia number shown in **f** (*Sun1b*$^{+/+}$, 4 fish; *Sun1b*$^{sa33109/sa33109}$ MO, n=4 fish; 3 areas measured/fish). **(e)** Quantification of average filopodia length shown in **f** (*Sun1b*$^{+/+}$, 4 fish; *Sun1b*$^{sa33109/sa33109}$ MO, n=4 fish; 3 areas measured/fish). Statistics: student's two-tailed *t* test. **; $p \leq 0.01$, ****; $p \leq 0.0001$. **(i)** Stills from Movie S3 and Movie S4 showing ISV

bioRxiv preprint doi: https://doi.org/10.1101/2021.08.11.455980; this version posted August 11, 2021. The copyright holder for this preprint (which was not certified by peer review) is the author/funder, who has granted bioRxiv a license to display the preprint in perpetuity. It is made available under aCC-BY-NC-ND 4.0 International license.

sprouting from 26 hpf to 36 hpf in zebrafish embryos with indicated morpholino treatment; anterior to left. *Tg(fli:LifeAct-GFP)* (green, vessels). Arrow points to sprout that does not connect to DLAV, although posterior ISVs make a connection. Scale bar, 20µm. **(j)** Quantification of ISV connection to DLAV shown in **i**. Data compiled from N=2 replicates (NT, n=6 fish, 32 ISVs; SUN1 MO, n=6 fish, 36 ISVs). Statistics: χ^2 analysis. **(k)** Model describing proposed role of nuclear SUN1 in angiogenic sprouting and endothelial cell junction stabilization.

Figure S1. Strategy for generation of *Sun1*^{iECKO} mice.

(a) Schematic showing strategy for generation of the *Sun1* floxed allele and subsequent Cre-mediated excision of exon 4 of the *Sun1* allele. **(b)** Agarose ethidium bromide gel showing PCR bands specific for WT or *Sun1*^{fl} allele.

Figure S2. SUN1 and SUN2 are nuclear localized in endothelial cells and do not regulate proliferation.

(a) Representative images of HUVEC with indicated siRNAs and stained with the indicated antibodies. Endothelial cells were stained for DAPI (DNA), SUN1, and SUN2. Scale bar, 20µm. **(b)** Quantification of SUN1 expression shown in **a**. Expression is normalized to NT. Data compiled from N=11 replicates. **(c)** Quantification of SUN2 expression shown in **a**. Expression normalized to NT. Data compiled from N=11 replicates. Statistics: one-way ANOVA with Tukey's correction. ns, not significant; *, $p \leq 0.05$; ****, $p \leq 0.0001$. **(d)** Representative images of HUVEC with indicated siRNAs and EdU incorporation. Endothelial cells were stained for DAPI (DNA) and EdU. Scale bar, 20µm. **(e)** Quantification of percent EdU positive cells shown in **d**. Data compiled from N=2 replicates. **(f)** Representative images of HUVEC with indicated siRNAs and

bioRxiv preprint doi: https://doi.org/10.1101/2021.08.11.455980; this version posted August 11, 2021. The copyright holder for this preprint (which was not certified by peer review) is the author/funder, who has granted bioRxiv a license to display the preprint in perpetuity. It is made available under aCC-BY-NC-ND 4.0 International license.

Ki67 staining. Endothelial cells were stained for DAPI (DNA) and Ki67. Scale bar, 20μm. **(g)** Quantification of percent Ki67 positive cells shown in **f**. Data compiled from N=3 replicates. Statistics: student's two-tailed *t* test. ns, not significant.

Figure S3. SUN1 regulates endothelial cell barrier function.

(a) Representative images of HUVEC with indicated siRNAs cultured on biotinylated fibronectin and treated with streptavidin upon confluence. Endothelial cells were stained for DAPI (cyan, DNA), Streptavidin (green), and VE-cadherin (white, junctions). Insets show junctions. Scale bar, 20μm. **(b)** Quantification of streptavidin area shown in **a**. Representative replicate. N=4 replicates. Statistics: student's two-tailed *t* test. *, $p \leq 0.05$. **(c)** Representative images and graphs of HUVEC with indicated siRNAs showing VE-cadherin line scan quantification. Endothelial cells were stained with DAPI (cyan, DNA) and VE-cadherin (white, junctions). Yellow line indicates where line scan was taken. Arrows point to the area under the curve (AUC). Scale bar, 20μm.

Figure S4. SUN1 regulates the actin cytoskeleton in endothelial cells.

(a) Representative images of HUVEC with indicated siRNAs showing changes in actin structures at the cell periphery. Endothelial cells were stained for DAPI (cyan, DNA) and VE-cadherin (white, junctions). Insets show actin structures at periphery. Scale bar, 20μm. **(b)** Representative images of HUVEC with indicated siRNAs stained for ppMLC. Endothelial cells were stained for DAPI (cyan, DNA) and ppMLC (white). Scale bar, 20μm. **(c)** Representative images of HUVEC with indicated siRNAs and indicated treatments. Endothelial cells were stained for DAPI (cyan, DNA) and Phalloidin (white, actin). Insets show actin structures at periphery. Scale bar, 20μm. **(d)** Representative images of HUVEC with indicated siRNAs and indicated treatments. Endothelial cells

bioRxiv preprint doi: https://doi.org/10.1101/2021.08.11.455980; this version posted August 11, 2021. The copyright holder for this preprint (which was not certified by peer review) is the author/funder, who has granted bioRxiv a license to display the preprint in perpetuity. It is made available under aCC-BY-NC-ND 4.0 International license.

were stained for DAPI (cyan, DNA) and Phalloidin (white, actin). Insets show actin structures at periphery. Scale bar, 20μm.

Figure S5. SUN1 regulates endothelial cell microtubule dynamics.

(a) Quantification of α-tubulin area at the MTOC (microtubule organizing center) shown in **Fig 4c**. **(b-d)** See Methods for details of experiments and analysis. **(b)** Quantification of EB3 comet velocity from TIP tracking. Data compiled from N=2 replicates. **(c)** Quantification of EB3 comet growth lifetime from EB3 TIP tracking. Data compiled from N=2 replicates. **(d)** Quantification of displacement from EB3 TIP tracking. Data compiled from N=2 replicates. Statistics: one-way ANOVA with Tukey's correction. ns, not significant; *, $p \leq 0.05$; **, $p \leq 0.01$; ****, $p \leq 0.0001$

Movie S1. Control endothelial cells elongate in 3D sprouting assay.

3D sprouting angiogenesis of control (NT) HUVEC over 60h, showing elongation of NT sprouts. Scale bar, 50μm. Frames acquired every 30 min.

Movie S2. SUN1-depleted endothelial cells retract in 3D sprouting assay.

3D sprouting angiogenesis of SUN1 KD sprouts over 60h, showing retraction of SUN1 KD sprouts. Scale bar, 50μm. Frames acquired every 30 min.

Movie S3. Control zebrafish have normal ISV growth.

Movie taken from 26-36 hpf in *Tg(fli:LifeAct-GFP)* zebrafish embryos injected with a NT morpholino, showing elongation of ISVs and connection to the DLAV. A, anterior; P, posterior. Scale bar, 20μm. Frames acquired every 15 min.

bioRxiv preprint doi: https://doi.org/10.1101/2021.08.11.455980; this version posted August 11, 2021. The copyright holder for this preprint (which was not certified by peer review) is the author/funder, who has granted bioRxiv a license to display the preprint in perpetuity. It is made available under aCC-BY-NC-ND 4.0 International license.

Movie S4. Loss of SUN1 in zebrafish leads to abnormal ISV growth.

Movie taken from 26-36 hpf in *Tg(fli:LifeAct-GFP)* zebrafish embryos injected with a SUN1 morpholino, showing an ISV that fails to elongate and connect to the DLAV. A, anterior; P, posterior. Arrow points to ISV that does not elongate. Scale bar, 20μm. Frames acquired every 15 min.

a

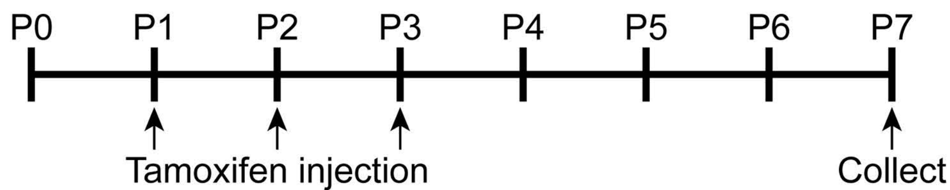

b

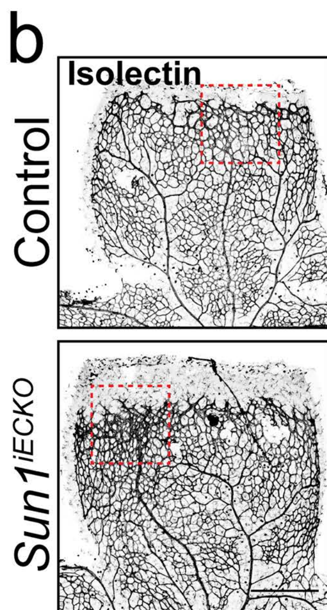

c

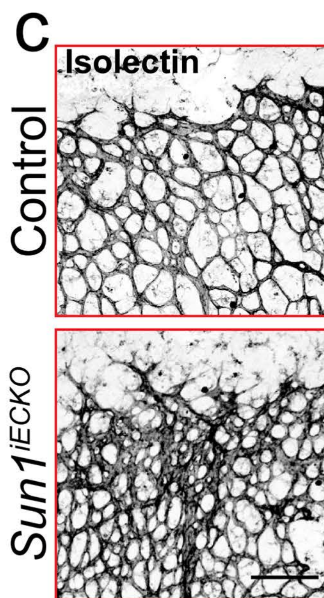

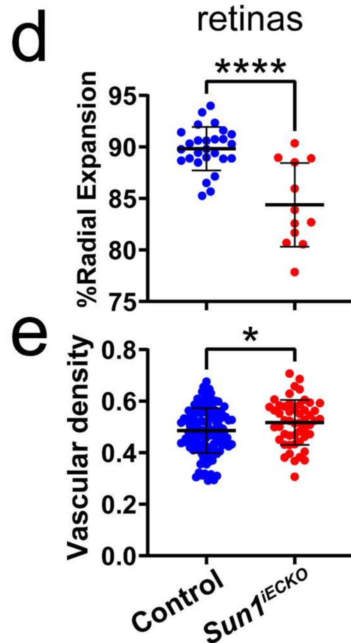

f

Isolectin

VE-Cadherin

Merge

Control

Sun1iECKO

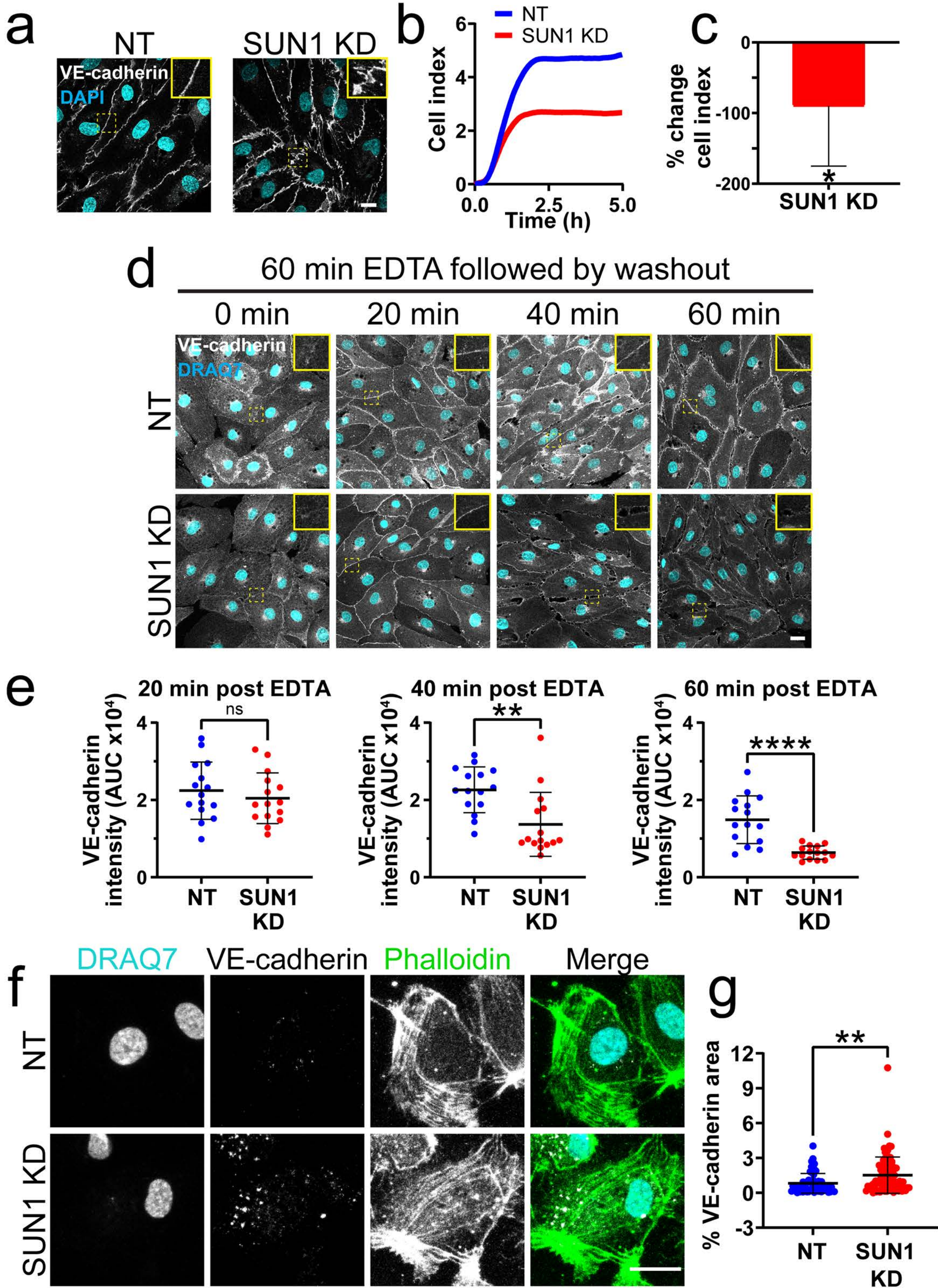
a
NT
SUN1 KD
VE-cadherin
DAPI
b
NT
SUN1 KD
Cell index
Time (h)
c
% change cell index
SUN1 KD
*
d
60 min EDTA followed by washout
0 min
20 min
40 min
60 min
VE-cadherin
DRAQ7
NT
SUN1 KD
e
20 min post EDTA
40 min post EDTA
60 min post EDTA
VE-cadherin intensity (AUC x10^4)
ns
**
****
NT
SUN1 KD
f
DRAQ7
VE-cadherin
Phalloidin
Merge
NT
SUN1 KD
g
% VE-cadherin area
**
NT
SUN1 KD

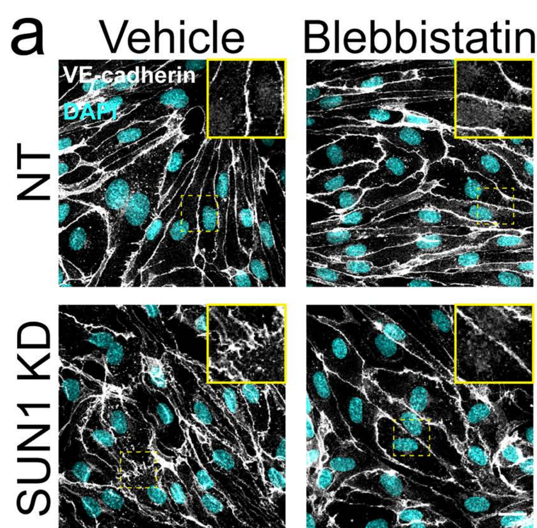
a
Vehicle
Blebbistatin
VE-cadherin
DAPI
NT
SUN1 KD

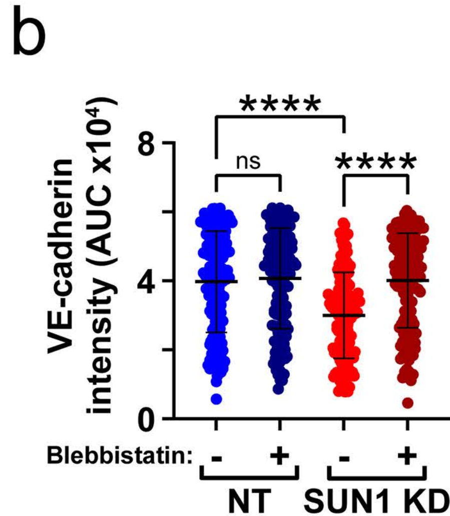
b
VE-cadherin intensity (AUC x10^4)
****
ns
****
8
4
0
Blebbistatin: - + - +
NT
SUN1 KD

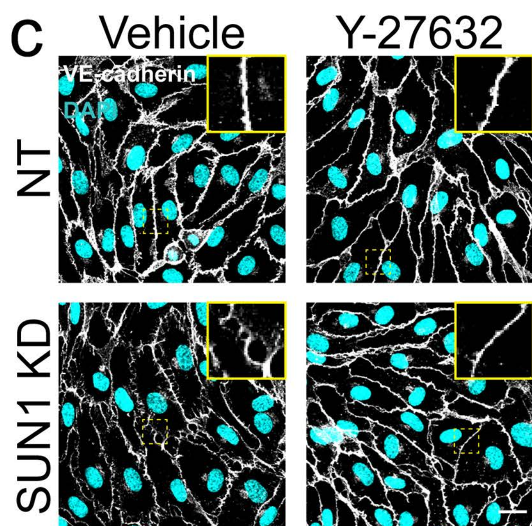
c
Vehicle
Y-27632
VE-cadherin
DAPI
NT
SUN1 KD

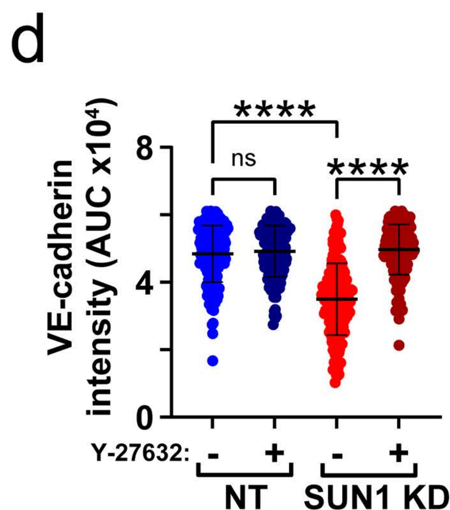
d
VE-cadherin intensity (AUC x10^4)
****
ns
****
8
4
0
Y-27632: - + - +
NT
SUN1 KD

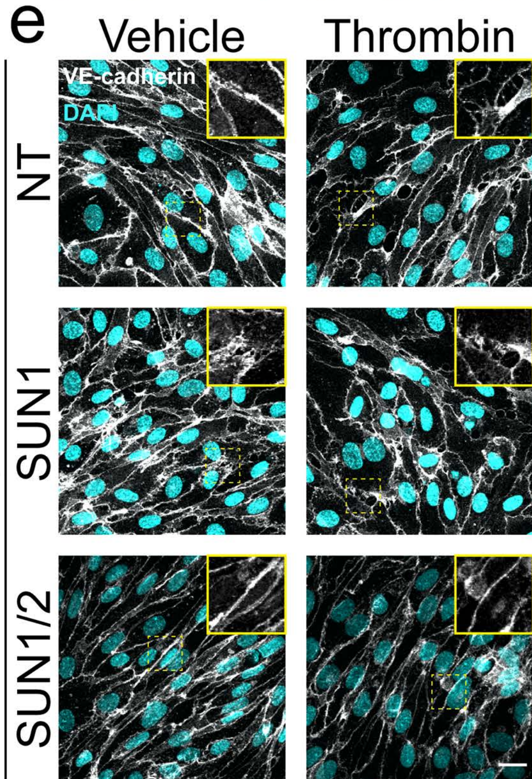
e
Vehicle
Thrombin
VE-cadherin
DAPI
NT
SUN1
SUN1/2
siRNA

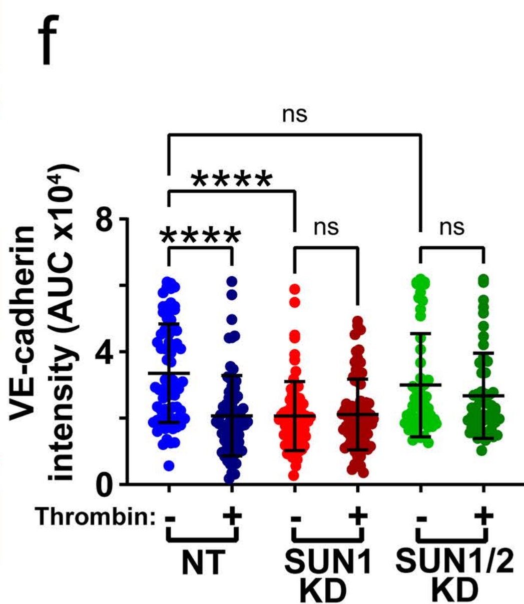
f
ns
****
****
ns
ns
VE-cadherin intensity (AUC x10^4)
8
4
0
Thrombin: - + - + - +
NT
SUN1 KD
SUN1/2 KD

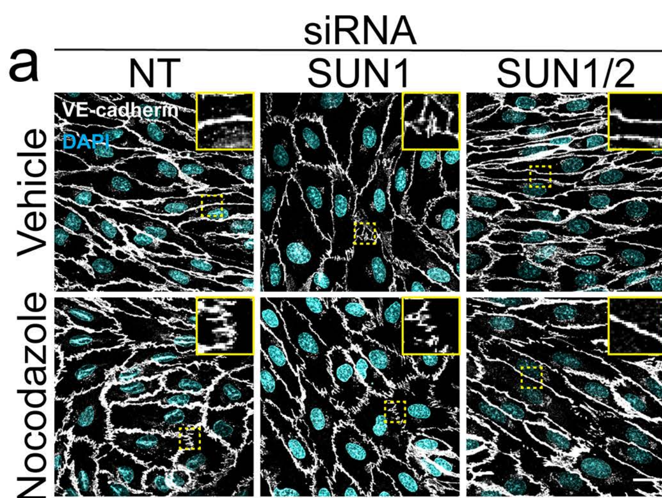

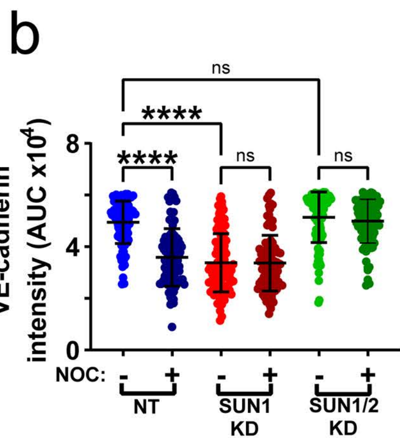

c

Merge DAPI VE-Cadherin α-tubulin Nuclear α-tubulin Peripheral α-tubulin

siRNA

NT

SUN1

SUN1/2

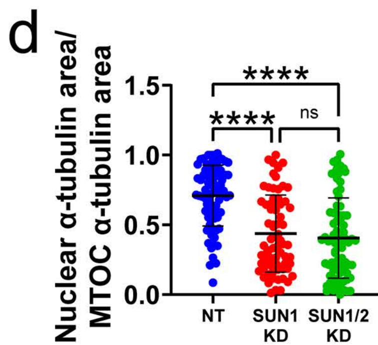

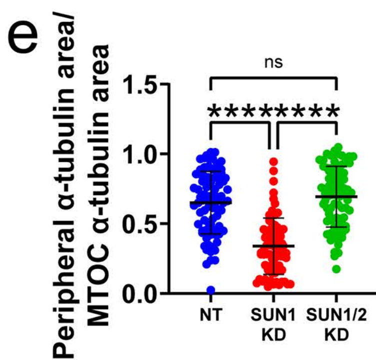

a

NT

SUN1 KD

Actin, Depth Encoded

b

Average sprout length (µm)

250
200
150
100
50
0

NT
SUN1 KD

****

c

Branches/mm

6
4
2
0

NT
SUN1 KD

****

d

0 h
10 h
20 h
30 h
40 h
50 h

NT

0.0 hr
10.0 hr
20.0 hr
30.0 hr
40.0 hr
50.0 hr

SUN1 KD

0.0 hr
10.0 hr
20.0 hr
30.0 hr
40.0 hr
50.0 hr

e

n=101 sprouts

n=77 sprouts

$p<0.001$

Extensions
Retractions

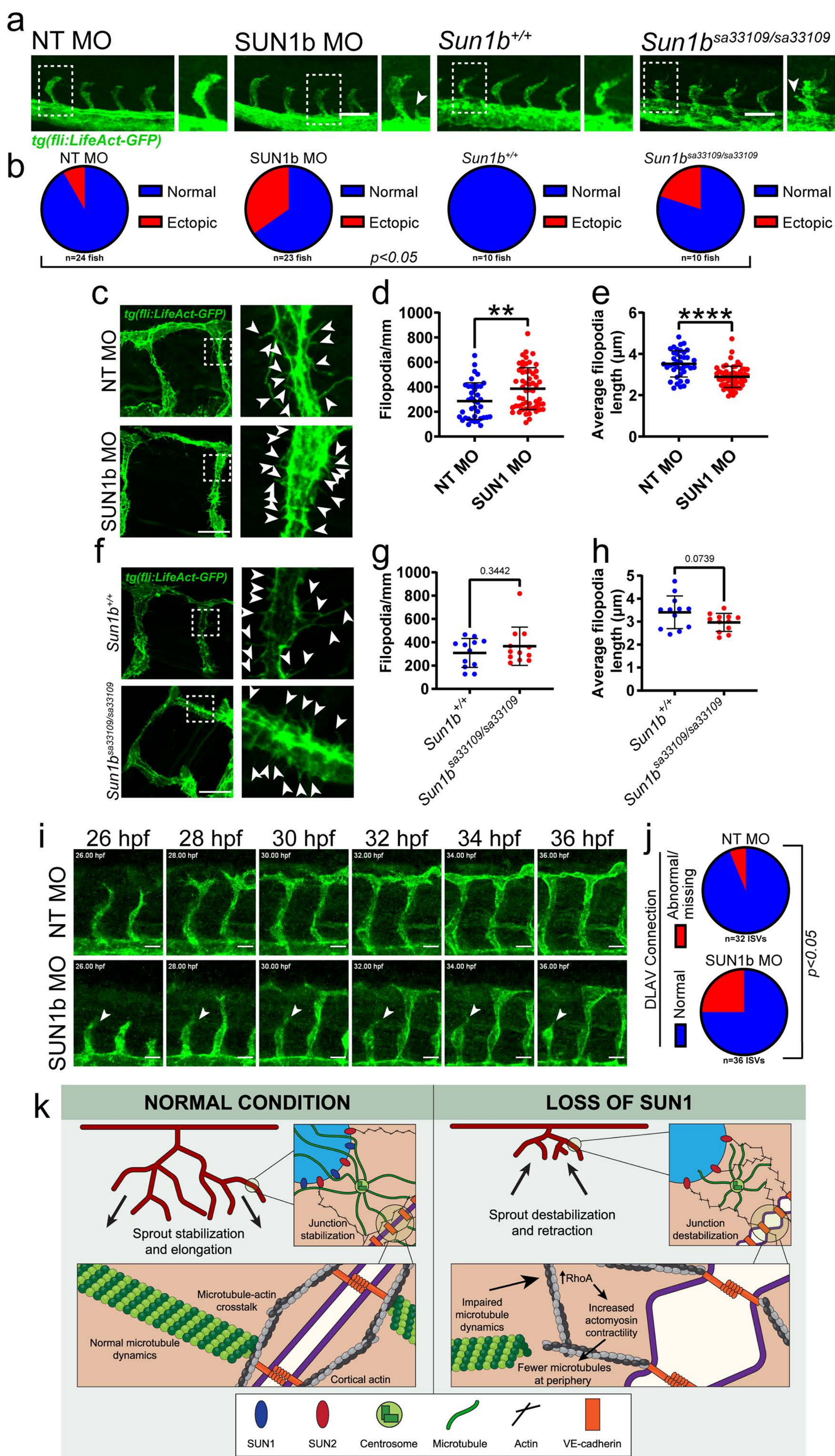

a
NT MO
SUN1b MO
Sun1b+/+
Sun1bsa33109/sa33109
tg(fli:LifeAct-GFP)
b
NT MO
Normal
Ectopic
n=24 fish
SUN1b MO
n=23 fish
p<0.05
n=10 fish
n=10 fish
c
d
e
tg(fli:LifeAct-GFP)
Filopodia/mm
Average filopodia length (μm)
**
****
NT MO
SUN1 MO
f
g
h
0.3442
0.0739
i
26 hpf
28 hpf
30 hpf
32 hpf
34 hpf
36 hpf
j
DLAV Connection
Abnormal/ missing
Normal
n=32 ISVs
n=36 ISVs
k
NORMAL CONDITION
LOSS OF SUN1
Sprout stabilization and elongation
Junction stabilization
Microtubule-actin crosstalk
Normal microtubule dynamics
Cortical actin
Sprout destabilization and retraction
Junction destabilization
↑RhoA
Impaired microtubule dynamics
Increased actomyosin contractility
Fewer microtubules at periphery
SUN1
SUN2
Centrosome
Microtubule
Actin
VE-cadherin